Air Force Institute of Technology
AFIT Scholar

Theses and Dissertations | Student Graduate Works

3-11-2011

A Multispectral Bidirectional Reflectance Distribution Function Study of Human Skin for Improved Dismount Detection

Bradley M. Koch

Follow this and additional works at: https://scholar.afit.edu/etd

Part of the Optics Commons

Recommended Citation

Koch, Bradley M., "A Multispectral Bidirectional Reflectance Distribution Function Study of Human Skin for Improved Dismount Detection" (2011). *Theses and Dissertations*. 1403.
https://scholar.afit.edu/etd/1403

This Thesis is brought to you for free and open access by the Student Graduate Works at AFIT Scholar. It has been accepted for inclusion in Theses and Dissertations by an authorized administrator of AFIT Scholar. For more information, please contact richard.mansfield@afit.edu.

www.manaraa.com

A MULTISPECTRAL BIDIRECTIONAL REFLECTANCE DISTRIBUTION FUNCTION STUDY OF HUMAN SKIN FOR IMPROVED DISMOUNT DETECTION

THESIS

Bradley M. Koch, Captain, USAF
AFIT/GE/ENG/11-22

DEPARTMENT OF THE AIR FORCE
AIR UNIVERSITY

AIR FORCE INSTITUTE OF TECHNOLOGY

Wright-Patterson Air Force Base, Ohio

APPROVED FOR PUBLIC RELEASE; DISTRIBUTION UNLIMITED

www.manaraa.com

The views expressed in this document are those of the author and do not reflect the official policy or position of the United States Air Force, the United States Department of Defense or the United States Government. This material is declared a work of the U.S. Government and is not subject to copyright protection in the United States.

www.manaraa.com

AFIT/GE/ENG/11-22

A MULTISPECTRAL BIDIRECTIONAL REFLECTANCE DISTRIBUTION FUNCTION STUDY OF HUMAN SKIN FOR IMPROVED DISMOUNT DETECTION

THESIS

Presented to the Faculty

Department of Electrical and Computer Engineering

Graduate School of Engineering and Management

Air Force Institute of Technology

Air University

Air Education and Training Command

in Partial Fulfillment of the Requirements for the

Degree of Master of Science in Electrical Engineering

Bradley M. Koch, B.S.E.E.

Captain, USAF

March 2011

APPROVED FOR PUBLIC RELEASE; DISTRIBUTION UNLIMITED

www.manaraa.com

AFIT/GE/ENG/11-22

A MULTISPECTRAL BIDIRECTIONAL REFLECTANCE DISTRIBUTION FUNCTION STUDY OF HUMAN SKIN FOR IMPROVED DISMOUNT DETECTION

Bradley M. Koch, B.S.E.E.
Captain, USAF

Approved:

Maj Michael J. Mendenhall, PhD Chairman	9 MAR 2011 Date
Dr. Michael A. Marciniak Member	9 Mar 11 Date
Dr. Michael T. Eismann Member	10 MAR 11 Date

Abstract

The war on terrorism has brought with it many challenges, one of which being combatants wearing no standard uniform and blending into the urban population. To assist with enemy detection and tracking, imaging systems that acquire spectral information bring to light many features in a scene which were once undetectable. Our research utilizes multispectral technology to better exploit naturally occurring phenomena to identify combatants.

In 2008, the Sensors Exploitation Research Group at the Air Force Institute of Technology began using spectral properties of skin for the detection and classification of humans. Since then, a multispectral skin detection system was developed to exploit the optical properties of human skin at wavelengths in the visible and near infrared region of the electromagnetic spectrum. A rules-based detector, analyzing an image spectrally, currently bases its skin pixel selection criteria on a diffuse skin reflectance model. However, when observing skin in direct view of the sun, a glint of light off skin is common and indicates specularity. The areas of skin with a high degree of specular reflectance result in misdetections. We show that skin is characterized by diffuse and specular reflectance, with both components dependent on the scene configuration. While we cannot always rely on the person to directly face the camera or have constant illumination conditions, it is important to have flexibility with the rules-based detector as the scene changes. Our research better characterizes skin reflectance as a function of source and detector angular locations to improve on the rules-based detector.

Our research approach first characterizes skin's specular reflectance with direct measurements. The fitting of a bidirectional reflectance distribution function model to

www.manaraa.com

the measurements with approximately 8.2% error allows us to incorporate the specular reflection component into the existing diffuse model. A method for extracting surface reflectance of a digitized three dimensional subject, paves the way for simulating many different conditions for a representative detection scenario. The result is a method to model the effects that changing scene configuration has on skin reflection and our ability to reliably do skin detection.

www.manaraa.com

Acknowledgements

I would like to thank all of those working at AFIT that had some part in making this time go by smoothly. The administrative staff, lab technicians, and faculty offered a professional atmosphere that created a great learning environment.

Special thanks to my thesis committee for accepting the role of approving authority over my research. Specifically my advisor Maj. Michael Mendenhall, your guidance kept me on the right track. Additionally, the courses taught by Dr. Michael Marciniak and Dr. Michael Eismann introduced me to many of the important concepts I needed for this research.

To my wife, your dedication in keeping the household running while I worked late into the night, contributed to my success. For my kids, I know it has been tough sharing me with school, but my time at home now is all yours again.

Bradley M. Koch

www.manaraa.com

Table of Contents

www.manaraa.com

Page

www.manaraa.com

Page

www.manaraa.com

List of Figures

www.manaraa.com

www.manaraa.com

www.manaraa.com

www.manaraa.com

www.manaraa.com

www.manaraa.com

www.manaraa.com

List of Tables

www.manaraa.com

List of Symbols

Symbol		Page
Φ_e	Flux in energy units	2-1
Φ_p	Flux in photon units	2-2
c	Speed of Light	2-2
h	Plank's constant	2-2
λ	Wavelength	2-2
M_e	Exitance	2-2
A_s	Source Area	2-2
E_e	Irradiance	2-2
Ω_d	Solid angle	2-2
L_e	Radiance	2-2
$L_e(\lambda)$	Spectral Radiance	2-3
T_{obj}	Temperature	2-3
ε	Emissivity	2-4
ρ	Reflectance	2-4
α	Absorbtance	2-4
τ	Transmittance	2-4
s_o	Object distance	2-6
s_i	Image distance	2-6
f	Focal Length	2-6
M	Magnification	2-6
A_{object}	object area	2-6
A_{image}	image area	2-6

www.manaraa.com

Symbol Page

www.manaraa.com

List of Abbreviations

www.manaraa.com

A MULTISPECTRAL BIDIRECTIONAL REFLECTANCE DISTRIBUTION FUNCTION STUDY OF HUMAN SKIN FOR IMPROVED DISMOUNT DETECTION

1. Introduction

Remote sensing is defined as "the field of study associated with extracting information about an object without coming into physical contact with it" [35]. Remote sensing is often used to scan a scene for a geological survey or gather intelligence with persistent monitoring of a remote area [29, 32]. The information gathered can be used to locate natural mineral deposits or disrupt a planned terrorist attack.

The human eye is a sensor that is similar to other optical sensors whereby photons are converted into an electrical signal for information processing [14]. While the eye is limited to visible wavelengths, much more information is available throughout the electromagnetic spectrum. With the availability of multispectral and hyperspectral systems, both spatial and spectral information for a scene are collected simultaneously. With added spectral dimensionality, objects that once blended into a scene for the human eye now become more distinguishable.

With most passive sensors used remotely, natural sources from the environment emit the observed radiation. The sun is often the greatest contributing source from visible (VIS) to near-infrared (NIR) wavelengths. Factors affecting the radiation reaching a detector are related to the atmospheric path and characteristic reflectance of in-scene objects. With prior knowledge of an object's reflectance spectra and atmospheric compensation techniques, an automated system can fill the requirement for the previously stated missions.

www.manaraa.com

1.1 Motivation

The current war on terror is an irregular war against an enemy that blends into the population. The threat is capable of concealing weapons and inflicting harm on the unsuspecting. The INSPIRE project is working to identify radical extremists with the integration of a sensor package to analyze human motion [22]. Since every individual has a specific walking pattern that changes when that individual is carrying a load, the INSPIRE team is building a database that records the gait cycle of human subjects with and without a load. The INSPIRE research has the potential of stopping those with harmful intent by tracking and recognizing a change in gait cycle.

The Civil Air Patrol (CAP) is a volunteer civilian auxiliary to the United States Air Force. One of its many missions is that of search and rescue. An addition to its support equipment for performing the search and rescue mission is the Airborne Real-time Cueing Hyperspectral Enhanced Reconnaissance (ARCHER) imaging system [6]. The ARCHER system currently compares reflected spectra to a library of previously measured data. Expanding its library to human skin spectra may improve its capabilities for locating people.

Human detection is an important first step to locating and tracking people's movement. Our research is working to save lives with an improved method for human detection.

1.2 Research Goals

To better detect people, we must accurately detect skin [8, 18, 28, 30]. We accomplish skin detection by exploiting its spectral reflectance at specific wavelengths in the VIS to NIR [28]. Limitations due to the scene configuration, e.g., lighting conditions and human orientation to the camera, drove a requirement to better characterize skin reflectance with changing conditions.

www.manaraa.com

Light reflecting off a surface may exhibit diffuse and/or directional behavior. Imperfections on the surface generally influence this behavior and is characterized by a Bidirectional Reflectance Distribution Function (BRDF), that may change with wavelength. As an example, consider small pebbles thrown toward a gravel surface, where the pebbles are much smaller in size. The pebbles likely bounce back at random directions, diffusely, depending on the slope of the gravel surfaces they impact. A basketball much larger in size thrown at the same surface, bounces back in a more predictable direction, specularly. While the surface looked rough to the small pebbles, it looked smooth to the basketball. In the same way electromagnetic radiation striking a surface reflects with wavelength analogous to size from the previous example [15]. In our case, we are observing light reflecting from skin. Therefore, characterizing surface reflectance of human skin, at our wavelengths of interest, is needed to better quantify skin apparent reflectance.

Prior research in [28] modeled subsurface skin reflectance with the limitation of normal incident illumination, resulting in a constant diffuse reflectance irrespective of illumination conditions. The diffuse reflectance values calculated for different skin types are then used as boundary conditions for a rules-based detector. We know from Fresnel's theory that reflectance at an interface changes as incident angle moves further off normal to the surface [16]. With Fresnel, the media refractive indices dictate the reflected light as a function of incident angle. For skin, some of the radiation transmits into the subsurface layers and reemerges, resulting in a combined subsurface and surface reflectance. The second goal of our work is to incorporate specular surface reflectance into the existing diffuse skin reflectance model. Application of the combined model is performed on a cylinder surface representing the shape of a persons face and neck, and then on a virtual scanned human.

Our research contribution is a more accurate skin reflectance characterization for

www.manaraa.com

the changing scene configuration. Better characterization of human skin reflectance for our VIS to NIR wavelengths used for detection serves to improve our spectral detection results of distinguishing between people and other objects in scene.

1.3 Thesis Overview

The remainder of this thesis is organized as follows. Chapter 2 is a review of background material on concepts that describe the nature of light, its interaction with media, and previous work on skin detection. The material in Chapter 2 is drawn from sources of literature by way of the engineering and physics community and is referred to throughout the document. Chapter 3 has the methodology and intermediate research results for characterizing human skin surface reflectance. The BRDF of human skin is characterized at our detection wavelengths and the environment for application is described. Chapter 4 presents measurements taken with the AFIT SERG multispectral system for off normal illumination. A comparison is made to a similar scenario simulated within animation rendering software. Chapter 5 summarizes the work accomplished in this thesis, its contribution to the research subject of dismount detection, and recommendations for future work. Appendices are included to show intermediate steps that are necessary to ensure accurate results in the following areas: geometric equations converting the global angular illumination onto a surface to a localized value with respect to a facet normal; BRDF of spectralon for different illumination conditions at 633 nm and 3390 nm; and methodology for extracting scene reflectance values from Blender simulations.

www.manaraa.com

2. Background

Chapter 2 covers concepts from published literature that are necessary to characterizing skin reflectance for detection. In Section 2.1, radiometric quantities are introduced as a foundation to the models developed for reflectance. Section 2.2, reviews optical concepts that apply to the design of the image-based Bidirectional Reflectance Distribution Function (BRDF) measurement system. In Section 2.3, there is an introduction to BRDF that includes a review of relevant literature in modeling and measurement which is later applied in our research to skin. Section 2.4, reviews the skin reflectance model in [28] developed by the Air Force Institute of Technology (AFIT) Sensors Exploitation Research Group (SERG) which is expanded on to include BRDF in Chapter 3. Finally, Section 2.5 introduces image processing tools used in skin detection.

2.1 Radiometry

Radiometry is the study of electromagnetic radiation measurement. Radiometric quantities from [13] describe a flux density quantitatively in order to gather information about a scene. With these quantites, a model is created to represent the configuration of a remote sensing scenario, and determine what is observed by a detector from self emitting and reflecting sources of radiation. Section 2.1 covers radiometry concepts used in our research for measurement and modeling of skin reflectance.

2.1.1 Radiometric Quantities.

Within radiometry, the most fundamental quantity, represented in energy units, is power or flux (Φ_e) in watts (W). The convention for choosing units is to relate them to the type of detector used for measurement, e.g., photon detectors respond

www.manaraa.com

directly to electron generation from incident photons. Quantities measured with photon detectors are set to photon units (Φ_p) in photons/s. With the following relationship, energy units are converted to photon units:

$$\Phi_q = \Phi_e \cdot \frac{\lambda}{hc}, \tag{2.1.1}$$

where c is the constant for the speed of light, h is Plank's constant, and λ is wavelength.

The radiometric quantities that facilitate in measurement and modeling are exitance, irradiance, and radiance. Exitance (M_e) in W/cm^2 is the flux leaving a source area (A_s), defined as:

$$M_e = \frac{\Phi_e}{A_s}. \tag{2.1.2}$$

Irradiance (E_e) in W/cm^2 is the flux falling on a surface area (A_d), defined as:

$$E_e = \frac{\Phi_e}{A_d}. \tag{2.1.3}$$

The flux leaving a source area per solid angle (Ω_d), measured in steradians (sr), is radiance (L_e) in W/cm^2-sr with a cosine correction of θ_s for off normal solid angles, defined as:

$$L_e = \frac{\Phi_e}{A_s \cos\theta_s \cdot \Omega_d}. \tag{2.1.4}$$

In Equation (2.1.4), a small angle approximation is assumed for $A_s \ll R^2$, where R is the range from the source area to the detector. Without the small angle approximation, flux is changing with respect to surface area and solid angle represented by:

$$L_e = \frac{\partial^2 \Phi_e}{cos\theta_s \partial A_s \partial \Omega_d}. \tag{2.1.5}$$

Given a known radiance, any other radiometric quantity is found by modifying Equa-

www.manaraa.com

tion (2.1.5). As seen in Equation (2.1.6), flux is isolated on the left side of the equal sign as:

$$\Phi_e = \int_{\Omega_d} \int_{A_s} L_e \cos\theta_s dA_s d\Omega_d, \tag{2.1.6}$$

thereby allowing the right side to be placed into Equation (2.1.2) or (2.1.3). With the flux substitution and a known scenario configuration, exitance and irradiance are solved from the known radiance.

While radiometric quantities vary with location, they also vary with wavelength. Referred to as spectral radiance ($L_e(\lambda)$), the total quantity is calculated at a specific wavelength or integrated over the wavelength region of interest. The total radiance over the wavelength region of interest is calculated as:

$$L_e = \int_{\lambda_2}^{\lambda_1} L_e(\lambda) d\lambda. \tag{2.1.7}$$

Demonstrated in Section 2.1 is the flexibility of the fundamental radiometric terms. When transforming the quantities as shown, a model is created based on what is known and what is assumed.

2.1.2 Self Emitting Sources.

According to blackbody theory, an object at a specific temperature emits radiation as function of wavelength. The blackbody spectral radiance for an object at temperature (T_{obj}) is characterized by the following equation:

$$L_e(\lambda) = \frac{2hc^2}{\lambda^5 \left(e^{\frac{hc}{\lambda k T_{obj}}} - 1 \right)}. \tag{2.1.8}$$

www.manaraa.com

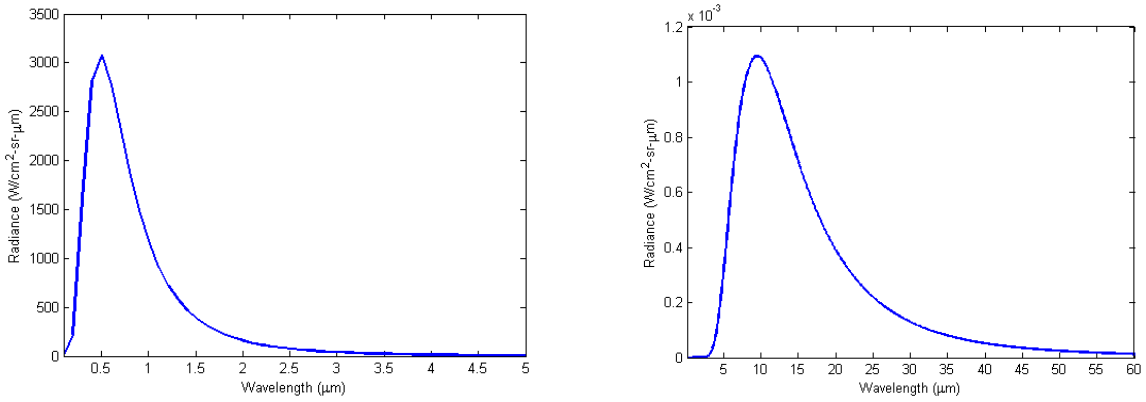

(a) (b)

Figure 1. Blackbody spectral radiance plots in energy units, for temperatures representing (a) the sun at 5950 K and (b) skin at 305 K.

The actual radiation emitted from an object is calculated as a fraction of the blackbody with the parameter emissivity (ε). The emissivity is either constant or varies with wavelength. In Figure 1, blackbody spectral radiance is plotted for 5950 K and 305K, temperatures for the sun and human skin. It is apparent that lower temperatures peak at higher wavelengths and higher temperatures peak at lower wavelengths. Self emitted radiation belonging to skin is negligible in the VIS to NIR wavelength region, while the self emitted radiation belonging to the sun contributes mostly in the VIS to NIR region.

2.1.3 Media Apparent Properties.

When electromagnetic radiation is incident on a media, it is partly reflected, absorbed, and transmitted. The percent of incident flux transformed is represented with the terms reflectance (ρ), absorptance (α), and transmittance (τ) defined as:

$$\rho = \frac{\Phi_{reflected}}{\Phi_{incident}}, \tag{2.1.9}$$

www.manaraa.com

$$\alpha = \frac{\Phi_{absorbed}}{\Phi_{incident}}, and \tag{2.1.10}$$

$$\tau = \frac{\Phi_{transmitted}}{\Phi_{incident}}. \tag{2.1.11}$$

Conservation of energy dictates that:

$$1 = \rho + \alpha + \tau, \tag{2.1.12}$$

and according to Kirchoff's law, in order for the object remain in thermal equilibrium, its emittance equals absorbtance [13].

The terms in Equation (2.1.12) represented spectrally, are instrumental to determining the flux transfer from a source to a detector. Ultimately, the observed flux density is characteristic of these media properties with which it interacts.

2.2 Optics

Geometric optics uses a treatment of radiation that is ideally imaged when propagated through a system, where a point in the object plane maps perfectly to a point in the image plane. Section 2.2 describes the optical components and theory to describe the propagation of light for imaging system design and radiative transfer.

2.2.1 Optical Components.

A lens and mirror are optical components that converge or diverge collected light. These components are used to image an object to a location described by the thin lens equation in [16]:

$$\frac{1}{s_i} + \frac{1}{s_o} = \frac{1}{f}, \tag{2.2.1}$$

www.manaraa.com

where s_o is the object distance, s_i is the image distance, and f is the focal length. The magnification (M) for the setup of a single optic is:

$$M = -\frac{s_i}{s_o}. \tag{2.2.2}$$

An object area A_{object} is imaged to an area A_{image} through an optical system with a magnification as:

$$A_{image} = M^2 \cdot A_{object}. \tag{2.2.3}$$

With these equations, optical components are positioned to create an imaging system. A focal plane array (FPA) placed at the image plane captures information from the object plane for the instantaneous field of view of each individual pixel.

2.2.2 Fresnel Equation.

With Fresnel equations, the amount of light reflecting from the front surface at the interface between two dielectric media is calculated [16]. The two media have indices of refraction n_1 and n_2, which may change with wavelength. The reflectance of incoming light normal to a dielectric surface is calculated as:

$$\rho_o = \left(\frac{n_2 - n_1}{n_2 + n_1}\right)^2. \tag{2.2.4}$$

At incident angles other than normal to the surface, the reflectance calculation for S and P polarization components are:

$$\rho_s(\theta_i) = \left(\frac{n_1 \cos\theta_i - n_2 \cos\theta_t}{n_1 \cos\theta_i + n_2 \cos\theta_t}\right)^2 and \tag{2.2.5}$$

$$\rho_p(\theta_i) = \left(\frac{n_1 \cos\theta_t - n_2 \cos\theta_i}{n_1 \cos\theta_t + n_2 \cos\theta_i}\right)^2. \tag{2.2.6}$$

www.manaraa.com

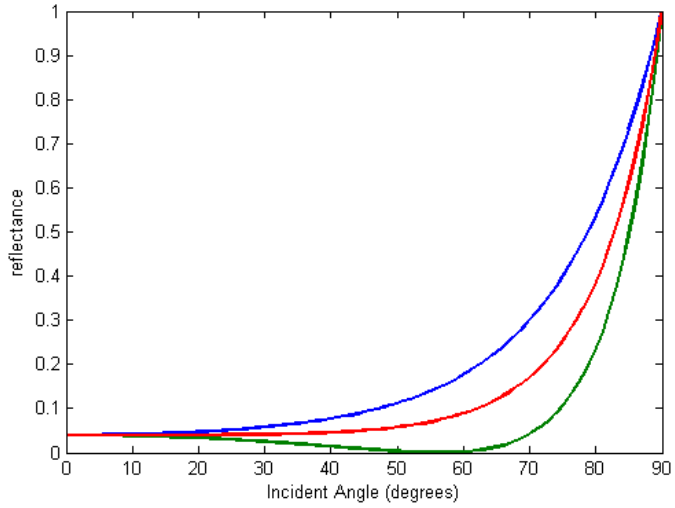

Figure 2. Reflectance calculated with Fresnel equations for the air to skin interface, showing S polarized (blue), P polarized (green), and unpolarized light (red) dependent on incident angle.

For unpolarized light, the reflectance is the average of Equations (2.2.5) and (2.2.6). In [28], an air ($n_1 = 1.0$) to skin ($n_2 = 1.5$) interface is calculated with Equation (2.2.4), resulting in a reflectance of 0.04. The off normal reflectance for the same air to skin indices applying Equations (2.2.5) and (2.2.6) is a function of incident angle, and is plotted in Figure 2.

Unpolarized reflectance calculated with Fresnel equations is often approximated with the following Schlick's model [34]:

$$\rho_{Schlick}(\rho_o, \theta_i) = \rho_o + (1 - \rho_o)(1 - \cos(\theta_i))^5 \tag{2.2.7}$$

where ρ_o is reflectance defined in Equation (2.2.4) and θ_i is the illuminated incident angle. In Figure 3, the Schlick approximation is shown in comparison to the unpolarized reflectance calculation from Fresnel dielectric equations.

www.manaraa.com

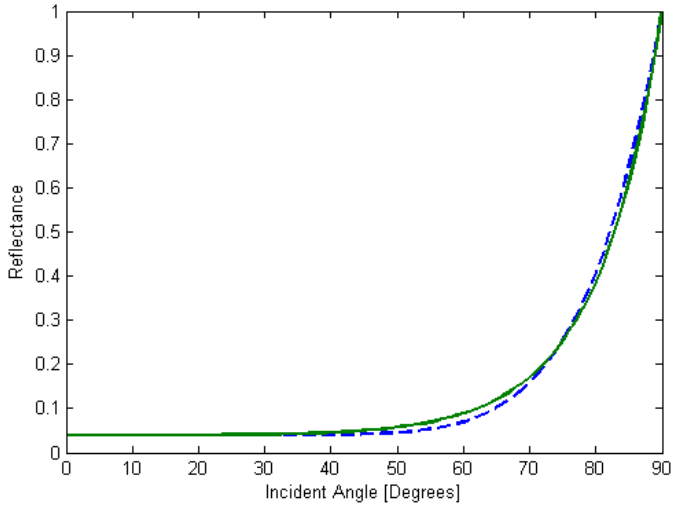

Figure 3. Unpolarized Fresnel reflectance (green) for the air to skin interface, compared with Schlicks approximation (blue) based on a normal incident reflectance of 0.04.

2.3 Bidirectional Reflectance Distribution Function (BRDF)

Most surfaces, natural and man made, are not perfectly smooth. At a microscopic scale, imperfections are seen along material surfaces. These surfaces reflect light to a location that is dependent on the angular direction of incoming light and the imperfection orientation. Meanwhile, a detector collects reflected light as a function of its size and location. An accurate characterization of material reflectance with these considerations is necessary for best estimation of apparent reflectance. The BRDF gives that characterization as a function of light source and detector configuration.

2.3.1 BRDF Background.

Three types of reflection are specular, diffuse, or a combination of specular and diffuse components. Specular reflection occurs with directional reflection of light from the surface, with incident angle equal to reflection angle. A material which best reflects specularly is a mirror. Diffuse reflection occurs with an equal spread of reflecting light in all directions from a surface. A theatre projector screen is an

www.manaraa.com

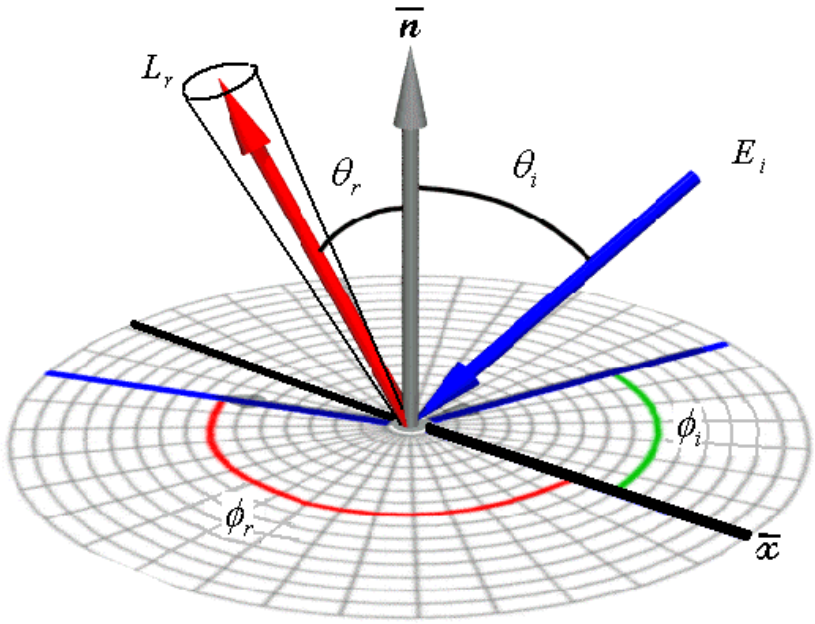

Figure 4. Diagram of of incoming irradiance and outgoing radiance in spherical coordinates from [5]. The out of plane nature with ϕ_i and ϕ_r about the x axis is shown along with the indicated incident θ_i and reflected θ_r angles from the surface normal n.

example of a diffuse material designed for all observers in the theatre to see the same image. The diffuse and specular combination has a spread of reflecting light about an illuminated surface, with an additional specular component. Most other surfaces from metal to vegetation fall into the diffuse and specular combination category.

BRDF (f_{BRDF}) in [36], characterizes reflectance with the following definition:

$$f_{BRDF}(\theta_i, \theta_r, \phi_i, \phi_r, \lambda) \triangleq \frac{L_r(\theta_r, \phi_r, \lambda)}{E_i(\theta_i, \phi_i, \lambda)}, \tag{2.3.1}$$

where the radiance leaving a surface over the irradiance onto the surface results in a reflectance per steradian measure, with associated angles shown in Figure 4. The BRDF is a distribution over the hemisphere and integrated over the detector solid angle to calculate the apparent reflectance. A common measure of a diffuse material is the reflectance over the entire hemisphere, named Directional Hemispheric Reflectance

www.manaraa.com

(DHR):

$$\rho_{DHR}(\theta_i, \phi_i, \lambda) = \int_0^{2\pi} \int_0^{\frac{\pi}{2}} f_{BRDF}(\theta_i, \theta_r, \phi_i, \phi_r, \lambda) \cos\theta_r \sin\theta_r d\theta_r d\phi_r. \tag{2.3.2}$$

2.3.2 BRDF Measurement Techniques.

Measuring the complete BRDF of a material is time consuming. In most cases, conditions are chosen to suit the application. BRDF is a subset of the bidirectional scatter distribution function which includes reflectance and transmittance. For our application, we do not measure transmittance since we only need to characterize reflectance. Our simplification eliminates an entire hemisphere of measurements on the other side of a surface. The BRDF can also vary over a spectrum of wavelengths. Specific wavelengths of interest are normally chosen to limit the amount of time needed to measure all wavelengths over an area of the spectrum of interest. Even with the described subset of conditions, it can take several days to collect data. For our research, it is not practical for a living subject to sit still for an extended period of time while data is collected. Section 2.3.2 reviews published literature describing some of the current BRDF measurement techniques.

A gonioreflectometer is a specialized measurement device used to collect BRDF data. The major components of the gonioreflectometer setup are the radiating source with optics, motorized armature with detector, mounted sample, and data acquisition equipment. With the system, the detector rotates around the sample with the source set to a fixed incident angle. When collecting data, the reflected energy is collected over the 90 degrees from the sample normal. The process is repeated for each angle of incidence over the 90 degrees about the sample. For out of plane measurements, a full 180 degree span is covered for each set of incident and reflected angles. With 10 degree angular steps, it adds up to 1,458 data points for each wavelength of interest.

www.manaraa.com

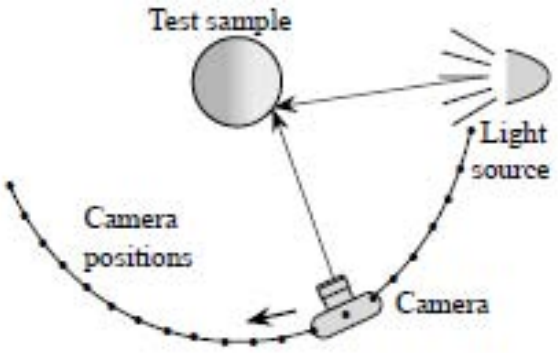

Figure 5. Image from [37] demonstrating the application of an image-based measurement system for characterizing BRDF of a cylindrical shape. The camera rotates around the cylinder, collecting reflecting light from a stationary source.

A higher fidelity data collection at 1 degree steps increases to 1,458,000 data points at each wavelength of interest.

A novel approach from [12, 37] uses an image-based technique to capture many of these data points simultaneously, which reduces the data collection time. By introducing a camera with an array of pixels to replace a single detector, each pixel acts as a detector for the BRDF measurement seen in Figure 5. In [37], they illuminate isotropic curved samples and use a camera to take pictures as they rotate the camera around the sample. With the symmetry of the sample and the camera pixel specifications known, they map the individual pixels to an area on the sample. They then calibrate the source and detector to determine the reflectance per steradian. They claim any curved surface can be sampled with the use of a range scanner to exactly describe the object orientation.

In [12], they use a parabolic mirror to direct incident rays to a single point on the sample located at the focal point of the mirror seen in Figure 6. Scattered rays from the sample collimate upon contact with the parabolic mirror. A camera is positioned in the path of these collimated rays to collect the data. The camera pixels are mapped to the parabolic mirror to determine reflection angle from the sample. The incident

www.manaraa.com

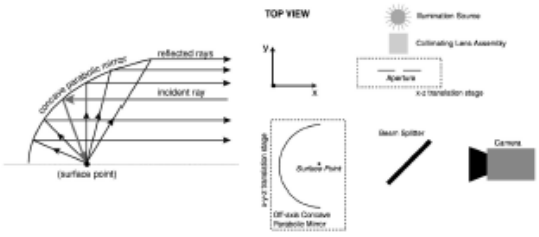

Figure 6. Image from [12] demonstrating the application of an image-based measurement system for characterizing BRDF onto a flat sample placed at the focal point of a parabolic mirror. The rays reflecting from the sample at the focal point collimate when incident on the mirror, which is then directed to the camera.

ray can be shifted to change the incident angle directed to the sample.

In order to accurately estimate radiometric quantities for in-scene objects, techniques described in Section 2.3.2 are applied in [37, 40, 41] for measuring skin BRDF. Since it is nearly impossible to measure every condition, models are fit to the limited amount of measured data to describe the response. The next section focuses on common models representing BRDFs.

2.3.3 BRDF Modeling.

The need for high fidelity BRDF models has been largely driven by the computer graphics community, which is seen in recent animated movies. The goal of the movie industry is to render realistic three dimensional images from in-scene objects with predefined surface characteristics. Within our research, we work backwards by extracting the apparent properties of objects from a measured or rendered image [26]. In [17, 23, 25], skin reflectance is modeled from subsurface light transport equations using Monte Carlo methods. Our method for modeling skin utilizes a BRDF for characterizing the skin surface reflectance. First, some of the techniques commonly used for BRDF modeling are presented.

The simplest BRDF model to approximate surface reflectance is the Lambertian

www.manaraa.com

model [24]:

$$f_d = \frac{\rho_d}{\pi}. \tag{2.3.3}$$

The Lambertian model assumes diffuse light is scattered equally in all directions and not a function of position.

The microfacet model in [31] describes a rough surface as made up of microfacets with surface normals distributed with a Gaussian distribution and utilized in the following form:

$$f_s(\theta_i, \theta_r, \Delta\phi, \lambda) = \frac{\rho_{Schlick}(\rho_o(\lambda), \beta(\theta_i, \theta_r, \Delta\phi))}{8\pi\sigma^2(\lambda)\cos^4\theta(\theta_i, \theta_r, \Delta\phi)\cos\theta_i\cos\theta_r} e^{\frac{-\tan^2\theta(\theta_i,\theta_r,\Delta\phi)}{2\sigma^2(\lambda)}}. \tag{2.3.4}$$

with β and θ defined as:

$$\beta(\theta_i, \theta_r, \Delta\phi) = \frac{\cos^{-1}(\cos(\theta_i)\cos(\theta_r) + \sin(\theta_i)\sin(\theta_r)\cos(\Delta\phi))}{2}, \tag{2.3.5}$$

$$\theta(\theta_i, \theta_r, \Delta\phi) = \cos^{-1}(\frac{\cos(\theta_i) + \cos(\theta_r)}{2\cos(\beta(\theta_i, \theta_r, \Delta\phi))}). \tag{2.3.6}$$

The angles denoted θ_i and θ_r are the global incident and reflected angles to the surface, $\beta(\theta_i, \theta_r, \Delta\phi)$ is the angle of incidence onto a microfacet, and $\tan(\theta(\theta_i, \theta_r, \Delta\phi))$ is the local surface slope. The spectral terms for slope variance $\sigma^2(\lambda)$ represents roughness and $\rho_o(\lambda)$ normal incident reflectance are fit for a specific material. Each microfacet obeys Fresnel equations approximated by Schlick's model for unpolarized light represented by ρ_s, and Snell's Law of reflection for light about each local facet normal. Figure 7 demonstrates the in-plane plots of the microfacet model for 0, 20, 40, and 60 degree incident angles and variance of 0.01, 0.02, and 0.03. In the Figure 7 plots, a constant normal reflectance of 0.04 is chosen for the Gaussian function, but for a more accurate representation the parameters must be fit to measured data. In [39], Ward implemented the Gaussian model as a simple and physically representative

www.manaraa.com

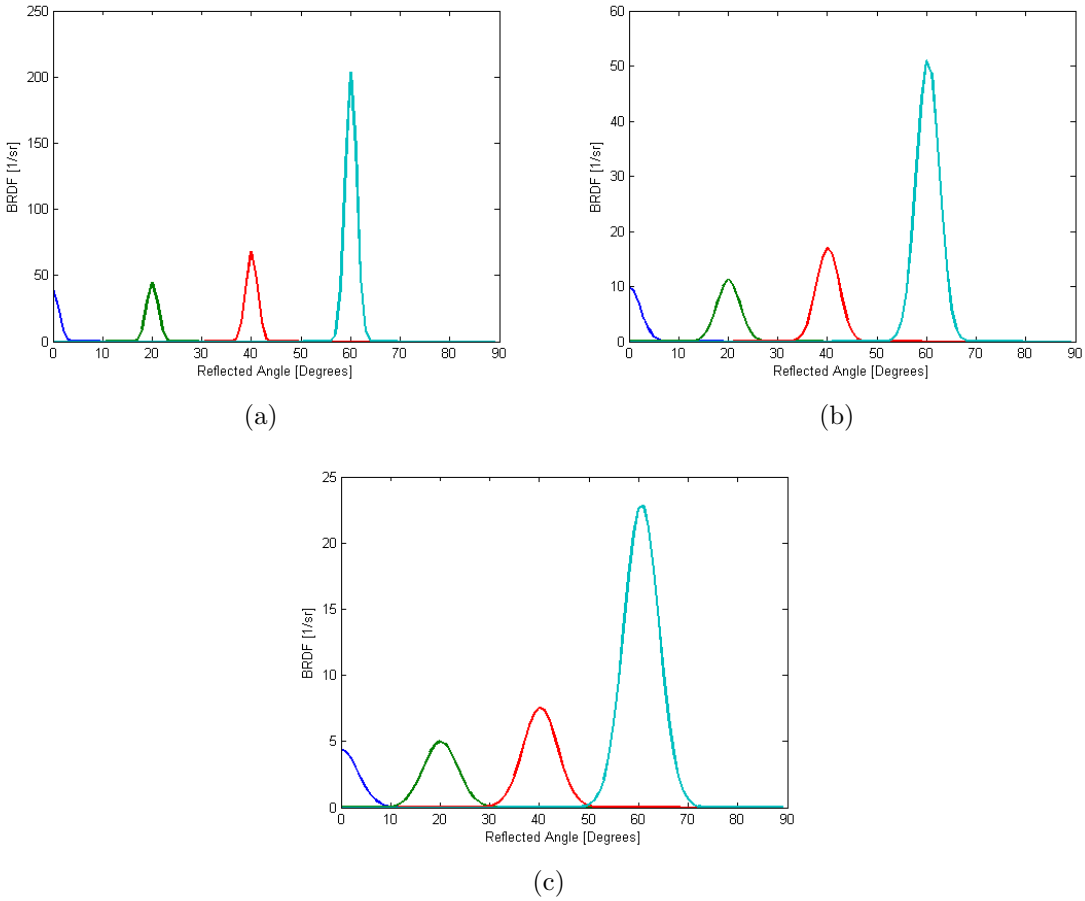

Figure 7. In-plane microfacet model, with set normal reflectance of 0.04 and variance of (a) 0.01, (b) 0.02, and (c) 0.03. The four different incident angles represented on each plot are 0 deg (dark blue), 20 deg (green), 40 deg (orange), and 60 deg (light blue).

rendering tool in graphics software.

Additional models relying on physical principals and data fitting are found in [10, 11, 21, 33, 38]. The models in [10, 11, 21, 33, 38] add additional fidelity to the microfacet model. The Torrence-Sparrow model adds a factor that accounts for shadowing from neighboring facets. The Maxwell-Beard model introduces a volumetric component that is attributed to subsurface reflectance. The Cook-Torrence model adds an ambient term from indirect sources. Over time, these models have been integrated into software packages such as Blender® and DIRSIG [2, 3]. With Blender

www.manaraa.com

and DIRSIG, an object is given reflectance characteristics for scenario modeling.

2.4 Human Skin

Skin is a complex material made up of different layers and physical parameters that affect reflectance, shown in Figure 8. The general structure of skin is the epidermis, dermis, and subcutaneous tissue. The epidermis is subdivided into five layers named the stratum corneum, stratum lucidum, stratum granulosum, stratum spinosum, and stratum basale. The dermis is subdivided into four layers named the papillary dermis, upper blood net dermis, reticular dermis, and deep blood net dermis. Within the layers are fractions of physical parameters of blood, water, collagen, melanosomes, hemoglobin, bilirubin, and betacarotene. Each layer described with these underlying components has a response to radiation that sums together to generate overall reflectance. Section 2.4 reviews the literature from [28] to describe the individual layer properties and build the existing skin reflectance model.

2.4.1 Optical Properties.

The radiation transfer through each layer is affected by absorption and scattering. Scattering occurs when traveling radiation impacts with a particle that is significant enough in size to cause a deviation in its course [16]. Scattering is dependent on wavelength of the traveling wave and the size of the particle it impacts. Different types of scattering contribute at different wavelengths such as Rayleigh and Mie scattering. To model scattering for each layer, a power law is fit in [28] allowing flexibility with a and b fitting parameters for each human subject:

$$s(\lambda) = a \cdot \lambda^{-b}. \tag{2.4.1}$$

The total absorption is additive of the absorption characteristics of physical pa-

www.manaraa.com

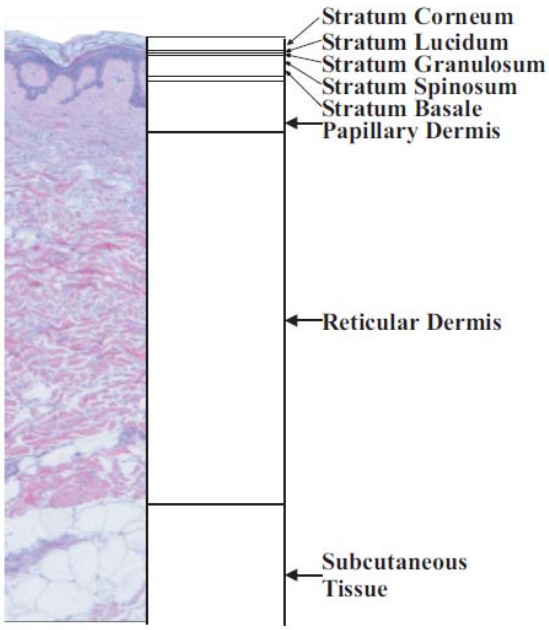

Figure 8. Layers of skin used in the Kubelka-Munk model for calculating diffuse reflectance [28].

rameters in each layer. The fraction of these parameters is unique for each individual person. The concentration parameters as a percentage of the nth layer of skin are represented by blood (b_n), water (w_n), collagen (c_n), melanosomes (v_n), and oxygenation fraction of blood (γ). Spectral absorption tables with units of cm^{-1}, empirically derived in [28] are collagen ($a_{col}(\lambda)$) , water ($a_{wat}(\lambda)$), betacarotene ($a_{car}(\lambda)$), bilirubin ($a_{bil}(\lambda)$), oxygenated hemoglobin ($a_{ohbl}(\lambda)$), and deoxygenated hemoglobin ($a_{dhbl}(\lambda)$). The absorption for melanosomes ($a_{mel}(\lambda)$), derived in [28] is:

$$a_{mel}(\lambda) = 6.6 \cdot 10^{11} \lambda^{-3.33} \tag{2.4.2}$$

The stratum corneum layer total spectral absoprtion in cm^{-1} is a combination of spectral absorption from percent concentrations of water, collagen, and betacarotene is described as:

$$a_1(\lambda) = c_1 a_{col}(\lambda) + w_1 a_{wat}(\lambda) + a_{ce}(\lambda) \tag{2.4.3}$$

www.manaraa.com

For the epidermis, $a_{ce}(\lambda)$ is the typical betacarotine spectral absorption in those layers with units of cm^{-1}. Layers 2 to 5 consist of percent concentrations with spectral absorption from water, collagen, and betacarotene described as:

$$a_n(\lambda) = v_n a_{mel}(\lambda) + c_n a_{col}(\lambda) + w_n a_{wat}(\lambda) + a_{ce}(\lambda) \tag{2.4.4}$$

Melanosomes are only in layers 4 and 5, all other layers v_n equals zero. The dermal layers of 6 to 9 consist of percent concentrations with spectral absorption in cm^{-1} of water, collagen, oxygenated hemoglobin, deoxygenated hemoglobin, bilirubin, and betacarotene, and they are described as:

$$\begin{aligned} a_n(\lambda) &= c_n a_{col}(\lambda) + (w_n + .9b_n)a_{wat}(\lambda) \\ &+(\gamma a_{ohb}(\lambda) + (1-\gamma)a_{dhb}(\lambda) + a_{car}(\lambda) + a_{bil}(\lambda))b_n \end{aligned} \tag{2.4.5}$$

Equations (2.4.3), (2.4.4), and (2.4.5) describe all the absorption features needed for subsurface skin reflectance modeling. Equation (2.4.1) is used for scattering in all layers except for the reticular dermis which is scaled by the fraction of collagen in that layer.

The absorption contributes to the characteristic shape of the overall reflectance and is an indicator when detecting a medium. At higher wavelenghts near 1400 nm, water is highly absorptive and the reflectance of skin is low. Another key feature is a characteristic W shape near 560 nm, due to oxygenated hemoglobin seen in Figure 9. The cadaver samples presented in [28] do not have a W feature due to the lack of oxygenated blood. In Figure 9, the shade of a person's skin is also evident and is directly related to melanosome content. Type V/VI skin, defined in Table 1, has a higher melanosome level leading to higher absorption in the visible wavelengths, while a lighter toned person is just the opposite.

www.manaraa.com

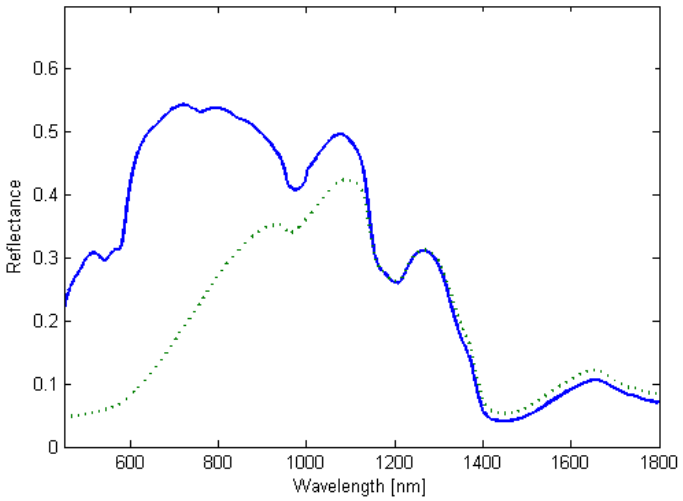

Figure 9. Radiometer measured skin reflectance of normally incident light, for Type I/II (blue) and Type V/VI (green) skin.

Table 1. Skin appearance as defined by the Fitzpatrick scale [27].

Skin Type	Skin Color
I	Very Fair
II	Fair
III	White to Olive
IV	Brown
V	Dark Brown
VI	Black

www.manaraa.com

These physical parameters play a key role in the development of the diffuse model component. All the spectral absorption data is documented in [28] and is needed to determine subsurface skin reflectance. The next section describes how the parameters are incorporated into the existing diffuse reflection model.

2.4.2 Diffuse Reflectance Modeling.

The Kubelka-Munk model from [9] describes the propagation of radiation through an isotropic slab of thickness d. The theory is applied to each of the nine layers of skin, and added with the surface normal Fresnel reflectance to generate a total reflectance from the skin. The absorption and scattering transport coefficients of Equations (2.4.1), (2.4.3), (2.4.4), and (2.4.5) are related to Kubelka-Munk parameters with the following relationship:

$$A_n(\lambda) = \frac{a_n(\lambda)}{\frac{1}{2} + \frac{1}{4}\left(1 - \frac{s_n(\lambda)}{s_n(\lambda)+a_n(\lambda)}\right)}, \tag{2.4.6}$$

$$S_n(\lambda) = \frac{s_n(\lambda)}{\frac{4}{3} + \frac{38}{45}\left(1 - \frac{s_n(\lambda)}{s_n(\lambda)+a_n(\lambda)}\right)}. \tag{2.4.7}$$

Equations (2.4.6) and (2.4.7) are the Kubelka-Munk transformed absorption and scattering coefficients that correspond to the specific case of an isotropic media. The Kubelka-Munk equations for reflectance and transmittance of a single layer are:

$$r_n(\lambda) = \frac{\sinh(S_n(\lambda)y_n(\lambda)d_n)}{x_n(\lambda)\cosh(S_n(\lambda)y_n(\lambda)d_n) + y_n(\lambda)\sinh(S_n(\lambda)y_n(\lambda)d_n)}, \tag{2.4.8}$$

$$\tau_n(\lambda) = \frac{y_n(\lambda)}{x_n(\lambda)\cosh(S_n(\lambda)y_n(\lambda)d_n) + y_n(\lambda)\sinh(S_n(\lambda)y_n(\lambda)d_n)}, \tag{2.4.9}$$

www.manaraa.com

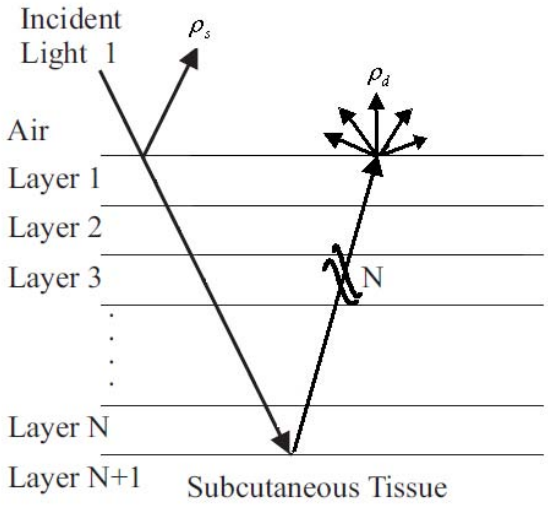

Figure 10. Conceptual drawing of suface and subsurface reflectance from multi-layered skin. The Kubelka-Munk model calculates a diffuse reflectance value that accounts for characteristics of each layer with the resulting energy emerging diffuse as it would from a bulk material [28]. The BRDF is used to calculate the specular reflectance component dependent on the surface geometry.

where x and y are defined as:

$$x_n(\lambda) = \frac{A_n(\lambda) + S_n(\lambda)}{S_n(\lambda)}, \tag{2.4.10}$$

$$y_n(\lambda) = \sqrt{x_n(\lambda)^2 - 1}. \tag{2.4.11}$$

While the reflectance and transmittance of a layer is calculated from Equations (2.4.8) and (2.4.9), there are additional reflectance and transmittance terms from the infinite interface bounces. When accounting for the additional bouces, the resulting recursive equations for the accumulated reflectance and transmittance of a single layer, seen in Figure 10, are:

$$R_{n+1}(\lambda) = R_n(\lambda) + \frac{T_n(\lambda)^2 r_{n+1}(\lambda)}{1 - r_{n+1}(\lambda)R_n(\lambda)}, \tag{2.4.12}$$

$$T_{n+1}(\lambda) = \frac{T_n(\lambda)\tau_{n+1}(\lambda)}{1 - r_{n+1}(\lambda)R_n(\lambda)}. \tag{2.4.13}$$

www.manaraa.com

The term for reflectance in Equation (2.4.12) is based on the transmittance and reflectance from the previous layer. The initial reflectance (R_0) is at the skin surface and is calculated as normal illuminated reflectance ρ_o from Fresnel Equation (2.2.4). The transmittance (T_0) into the first layer is calculated from 1 - R_0. The calculations continue with the next layers until we reach the subcutaneous fat which has reflectance from measured values in [28]. The result is a reflectance that emerges and is characteristic of all skin layers.

2.4.3 Fitting Model to Measurements.

The Kubelka-Munck model developed in [28], has physical parameters that are fit to a specific person. Adjusting these parameters allows us to generate reflectance values that match with measured data creating a general model for that person. The fitting parameters are melanosomes fraction, blood level, blood oxygenation, reticular dermis depth, collagen fraction, and subcutaneous scale. The physical parameters kept constant are the layer depths (excluding reticular dermis), water percentage in each layer, and blood percentage. In [28], these parameters were shown to be standard values for each person.

To fit a model to measured data, a quantitative method is used to provide a measure of difference between the them. A common error function is the root mean square error (RMSE):

$$RMSE(\lambda) = \sqrt{\frac{1}{N}\sum \left(\rho(\lambda)_{model} - \rho(\lambda)_{measure}\right)^2} \tag{2.4.14}$$

which is applied repeatedly, while changing parameter values until the minimum error between the measured and modeled reflectance is found. This approach use and optimization search strategy with matlab. In Equation (2.4.14), N represents the number of wavelength bands the reflectance is summed over.

www.manaraa.com

2.5 Radiative Transfer and Detection

Since all media have their own unique spectral properties, the process of detecting a specific medium is made easier by collecting the spectral content of a scene. A problem with searching a scene in order to locate a specific signature is that illumination conditions and path losses affect what is observed by the detecting system. Section 2.5 reviews image processing techniques and radiative transfer modeling supporting skin detection.

2.5.1 Radiative Transfer Modeling.

Radiative transfer modeling is a method for predicting remotely observed spectral radiance based on scene and atmospheric properties. Characterizing a remote sensing scenario with radiometric terms allows tracking of flux along a path from the source to the detector.

The operating band of the detector is important for modeling sources of radiation affecting the system. Looking back at the blackbody radiation curve in Figure 1, it is clear the sun dominates in the visible and NIR bands while lower temperature self emitting objects contribute most from the NIR to long wave infrared. Additionally, path losses are attributed to the atmospheric conditions which change daily. MODTRAN is a modeling tool that can generate path radiance and losses for the specified atmospheric conditions. With these considerations, a simple diffuse model for radiance at the aperature of a visible to NIR detection system, estimating medium self-emission negligible, is defined as:

$$L_e(\lambda) = \tau_a(\lambda) \cdot \frac{\rho(\lambda)}{\pi} \cdot E_i(\lambda) + L_a(\lambda), \tag{2.5.1}$$

where L_a and τ_a are atmospheric radiance and transmittance, E_i is incident irradiance

www.manaraa.com

onto the medium surface, and ρ is the medium reflectance. In [30], the radiometric model used for our multispectral skin detection system is:

$$\Phi_{p-pixel} = \int_{400nm}^{1700nm} L_{e-target}(\lambda)\Omega_{pixel}A_{opt}\tau_{atm}(\lambda)\tau_{opt-filter}(\lambda)\frac{\lambda}{hc}\tau_{int}(\lambda)\eta(\lambda)d\lambda \quad (2.5.2)$$

where τ_{atm} is atmospheric transmittance, $\tau_{opt-filter}$ is optical filter transmittance, τ_{int} is integration time, Ω_{pixel} is pixel solid angle, A_{opt} is area of the optic, and η is quantum efficiency. For the specific case of a Lambertian target, the radiance is substituted with:

$$L_{e-target}(\lambda) = E_{e-target}(\lambda) \cdot \frac{\rho(\lambda)}{\pi}. \quad (2.5.3)$$

2.5.2 Empirical Line Method (ELM).

While path characteristics of a scene are not always known, the Empirical Line Method (ELM) was developed to estimate and compensate for these path effects. In Equation (2.5.1), a general radiative transfer model was introduced with variables that are lumped into the following form:

$$L_e(\lambda) = a(\lambda) \cdot \rho(\lambda) + b(\lambda). \quad (2.5.4)$$

For two in-scene media of known reflectance and measured radiances, the remaining linear constants a and b are solved as:

$$a(\lambda) = \frac{L_2(\lambda) - L_1(\lambda)}{\rho_2(\lambda) - \rho_1(\lambda)}, \quad (2.5.5)$$

$$b(\lambda) = \frac{L_1(\lambda) \cdot \rho_2(\lambda) - L_2(\lambda) \cdot \rho_1(\lambda)}{\rho_2(\lambda) - \rho_1(\lambda)}. \quad (2.5.6)$$

www.manaraa.com

For uniform illumination of the scene, the remaining measured data is mapped from radiance to reflectance as:

$$\rho(\lambda) = \frac{L_e(\lambda) - b(\lambda)}{a(\lambda)}. \tag{2.5.7}$$

2.5.3 Skin Detection.

2.5.3.1 Basic Skin Detector.

While observing landcover with space-based imaging systems, a efficient method was developed that indicated vegetation named Normalized Difference Vegetation Index (NDVI) [4]. As seen in Figure 9, there are characteristic dips specific to skin, similar to vegetation, which lead to the development of the Normalized Difference Skin Index (NDSI) in [28]. Identifying the large difference in skin reflectance at 1080nm and 1580nm drove the following form of NDSI:

$$\gamma = \frac{\rho(1080nm) - \rho(1580nm)}{\rho(1080nm) + \rho(1580nm)}, \tag{2.5.8}$$

where large NDSI values are an indicator of skin. As a secondary measure for detecting skin, the Normalized Difference Green Red Index (NDGRI) is used. Since there is a large difference in reflectance between the red and green colors of skin it is defined as:

$$\beta = \frac{\rho(633nm) - \rho(544nm)}{\rho(633nm) + \rho(544nm)}. \tag{2.5.9}$$

2.5.3.2 Rules-Based Detector.

With the basic detector of NDSI or NDGRI alone, objects with spectra similar to skin, such as vegetation, may confuse the detector. A rules-based detector from [28]

www.manaraa.com

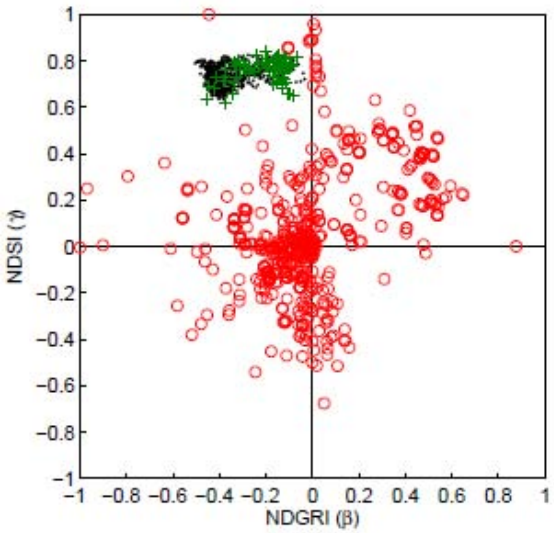

Figure 11. Scatterplot of the rules-based detector for living and cadaver measured skin from [28] (green) and diffuse modeled skin (black) ranging from Type I/II to Type V/VI. The red circles represent spectral confuser data from other objects. The grouping of skin pixels drive the boundary conditions for the rules-based detector.

was established to reduce false alarms. The rule is as follows:

$$S_{i,j} = \begin{cases} 1 \; if \; b_1 \leq \beta_{i,j} \leq b_2 \; and \; c_1 \leq \gamma_{i,j} \leq c_2 \\ 0 \text{ otherwise} \end{cases} \tag{2.5.10}$$

where β and γ are values computed per pixel in the NDSI and NDGRI Equations (2.5.8) and (2.5.9). A pixel is considered skin if it falls into the boundary and rejected as another object otherwise. The boundary conditions have been set by applying the diffuse skin model for different types of skin developed in [28]. The minimum and maximum values for NDSI and NDGRI associated with that model are b_1 = -0.54079, b_2 = -0.061525, c_1 = 0.65703, and c_2 = 0.76779. In Figure 11, a rules-based detector is demonstrated on diffuse modeled skin for the Type I/II to Type V/VI range represented by black dots, living and cadaver skin measurements from [28], and confuser objects in red circles. The rules-based detector applied to an image captured

www.manaraa.com

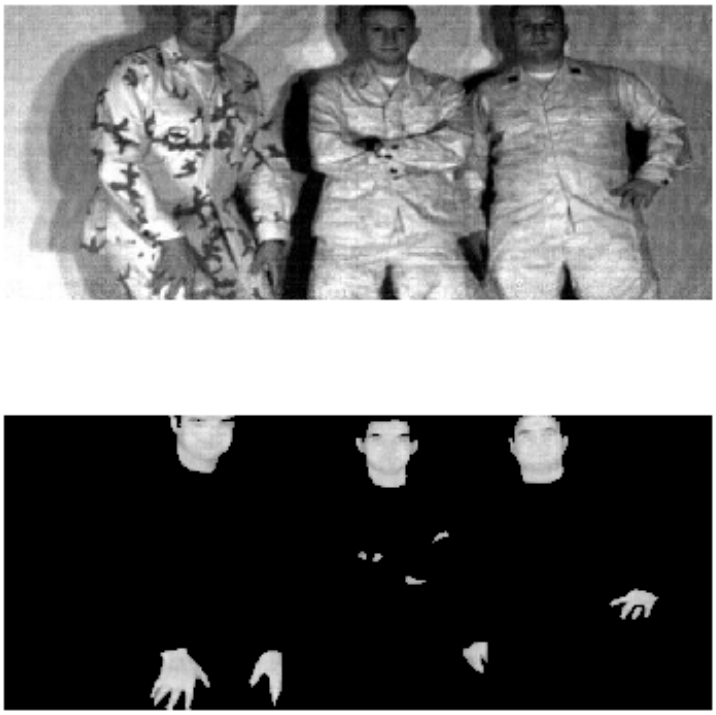

Figure 12. Image collected with the Hyper Spectir V3 HST3 imager [20]. (Top) Gray scaled image of the original snapshot. (Bottom) An image mask with applied rule based detector that displays pixels meeting criteria for skin.

with the Hyper SpecTIR V3 hyperspectral imager [20] is shown in Figure 12. The gray scaled image is above a mask that shows pixels meeting conditions for skin.

2.6 Summary

Chapter 2 introduced material that provides the foundation to all the modeling and measurements we use to characterize skin. The radiometry section defined all the terms used for the quantitative results. The human skin and BRDF sections gave detailed description of the models used for skin. The optics section provided the imaging equations used for the measurements systems. The final section described

www.manaraa.com

the image processing techniques for skin detection.

www.manaraa.com

3. Methodology

In Chapter 3, our method for characterizing surface reflectance and incorporating it into the existing diffuse skin reflectance model is shown. Intermediate results show our Bidirectional Reflectance Distribution Function (BRDF) measurements and the fit to BRDF models. The remaining chapter describes an environment for running the combined reflectance model on a geometry representing a person.

In Chapter 2, we introduced the rules-based detector for determining skin pixels in an image. The boundary conditions for NDGRI and NDSI are set from diffuse spectral reflectance values for the range of skin types determined in [28]. Dependent on the amount of specular reflection, the pixel may fall outside the bounds of the rule based detector and not be considered skin. The remaining chapter characterizes skin reflectance for changing illumination and detector conditions to improve the rules-based detector.

3.1 Combined Skin Reflectance Model

While the human body is uniquely shaped and dependent on the individual person, segments of the body follow a similiar form, e.g., the head is round, the back of the hand is relatively flat, and arms are cylindrical. To determine what is observed by a detector for a defined scene configuration, a combined skin reflectance model must be applied to human skin surface geometries. Section 3.1 develops the combined skin reflectance model for application to geometries that represent parts of the human body.

www.manaraa.com

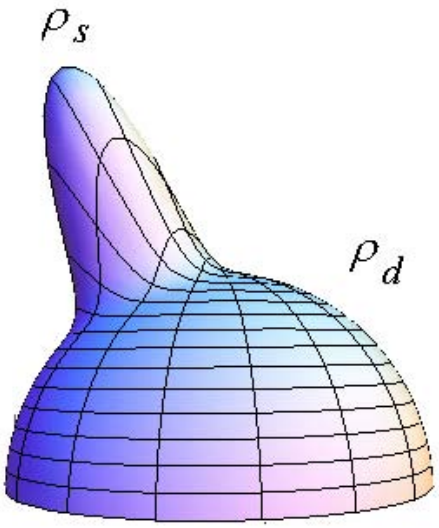

Figure 13. A graphic of the diffuse plus specular reflection model used to characterize human skin. The diffuse component is the constant hemispheric dome and the lobe depicts specular reflection.

3.1.1 Combined Reflectance Model Derivation.

When characterizing skin reflectance, it is best to directly measure the skin response to light, accomplished in a later section. For now, skin is considered neither perfectly diffuse or perfectly specular, so a general BRDF model combines both components as:

$$f_{BRDF}(\theta_i, \theta_r, \Delta\phi, \lambda) = \frac{\rho_{Schlick}(\rho_o(\lambda), \beta(\theta_i, \theta_r, \Delta\phi))}{8\pi\sigma^2(\lambda)\cos^4\theta(\theta_i, \theta_r, \Delta\phi)\cos\theta_i\cos\theta_r} e^{\frac{-\tan^2\theta(\theta_i,\theta_r,\Delta\phi)}{2\sigma^2(\lambda)}} + (1 - \rho_{Schlick}(\rho_o(\lambda), \beta(\theta_i, \theta_r, \Delta\phi)))\frac{\rho_d(\lambda)}{\pi}, \quad (3.1.1)$$

where the BRDF is the sum of specular (f_s) and diffuse (f_d) components from Equations (2.3.3) and (2.3.4), illustrated in Figure 13. The angles β and θ are defined in Equations (2.3.5) and (2.3.6). The Schlick's approximation is used as the proportionality term conserving energy between the diffuse and specular component. Both the slope variance and normal reflectance terms are now wavelengths dependent and

www.manaraa.com

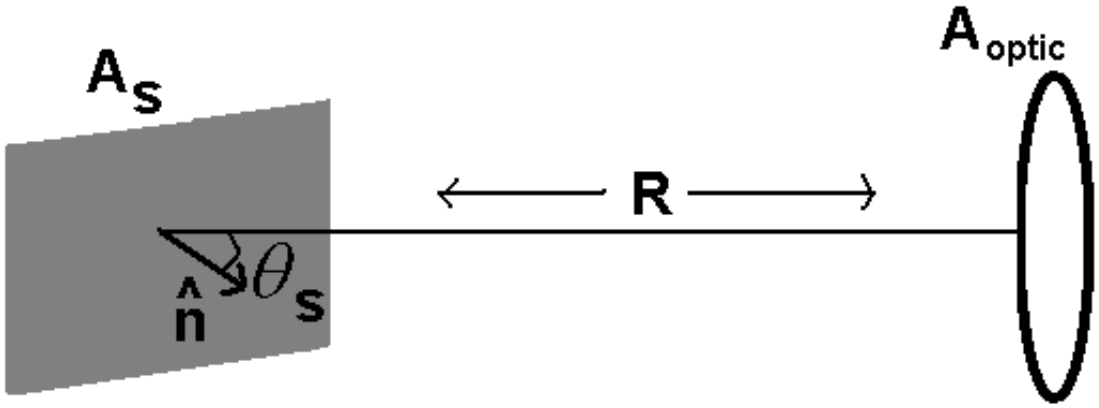

Figure 14. Diagram of our imaging system optic, viewing a surface that is rotated θ_s degrees. The surface reflectance component viewed by the imaging system is dependent on the parameters shown. The general layout is the same for all of our measurement scenarios.

set for the specific wavelength of interest. The specular component is represented by surface reflectance through a BRDF model described in Section 2.3. The diffuse component is represented by subsurface reflectance through radiometer measurements.

Once a BRDF is established, the surface reflectance component viewed by our imaging system can be calculated. The Directional Hemispheric Reflectance (DHR) from Equation (2.3.2) is a standard integration to make that conversion, representing surface reflectance into the entire hemisphere above a media surface. However, the DHR does not differentiate between locations of specular and diffuse reflection for a discrete solid angle of a detector. To more accurately characterize combined reflectance observed by a detector, the combined reflectance is calculated over the detector solid angle instead of the entire hemisphere. The diagram in Figure 14 illustrates the desired parameters for our modeling calculations and is similar to the experimental scenario collections. For the surface reflectance of Figure 14, the definition for BRDF is restated to solve for radiance from the surface, which is then

www.manaraa.com

substituted into the equation for flux, Equation (2.1.6) as:

$$L_r(\theta_i, \theta_r, \Delta\phi, \lambda) = f_{BRDF}(\theta_i, \theta_r, \Delta\phi, \lambda) E_i(\theta_i, \lambda), \tag{3.1.2}$$

$$\Phi_r(\theta_i, \theta_r, \Delta\phi, \lambda) = \int_{\Omega_d} \int_{A_s} f_{BRDF}(\theta_i, \theta_r, \Delta\phi, \lambda) E_i(\theta_i, \lambda) \cos\theta_r dA_s d\Omega_d. \tag{3.1.3}$$

Further modifying Equation (3.1.3) by dividing out incident flux and applying the small angle approximation, leads to the following form of combined reflectance observed by our multispectral system:

$$\rho_{combined}(\theta_i, \theta_r, \Delta\phi, \lambda) = f_{BRDF}(\theta_i, \theta_r, \Delta\phi, \lambda) \frac{A_{optic}}{R^2} \cos\theta_r. \tag{3.1.4}$$

Since the small angle approximation is used, reflectance over the field of view of the detector is approximated constant. The small angle approximation reduces complexity of the model by eliminating the need to integrate discretely over the surface area where each point on the surface has a small angular variation feeding into the BRDF model.

The subsurface reflectance measured with our radiometer and modeled with the Kubelka-Munk seen in [28] uses the assumption that light is normally incident to skin and the surface component is Lambertian. With the Lambertian assumption, the normally incident Fresnel reflection Equation (2.2.4) contributes a diffuse surface reflectance of 0.04 equally into the hemisphere above the skin surface. Since we are considering incident light off normal, we use the DHR to determine trasmittance into the first layer of skin by the law of energy conservation. The next sections go into detail on the specular and diffuse components, while the following subsections complete the discussion by describing an environment for application.

www.manaraa.com

3.1.2 Pixel Field of View.

When applying the small angle approximation, the area within the field of view of the detector is much smaller than the distance to the detector, therefore any change in location on the projected pixel results in a small change of angle along the center axis of the optic. With a magnified optical system, the detector projects using the lens Equation (2.2.3). Each individual pixel for a focal plane array, projects with the same lens equation. The center of the projected pixel is used to calculate distance to the lens and the plane whose local normal is the reference for incident and reflected angles of light.

3.1.3 Light Source.

In order to calculate combined reflectance as a function of incident angle, the incoming light rays are given the same directionality. Knowing the global angular direction of the incoming light enables us to calculate local angles for individual projected pixels.

3.1.4 Surface Modeling.

Individual projected pixels are used to form larger shapes, therefore we first introduce treatment of a single projected pixel. A projected pixel in Figure 15, is represented in two configurations with respect to the global reference axis. The left image is aligned with its normal along the reference axis, and the right image is rotated 45 degrees. For incoming light at 15 degrees to the right of the global reference axis, the left projected pixel incident angle is 15 degrees, while the right projected pixel incident angle is 60 degrees off the local normal. Similarly, reflected angle to a detector is with respect to the projected pixel normal. The incident and reflected angles for each projected pixel are used for calculating combined reflectance, therefore

www.manaraa.com

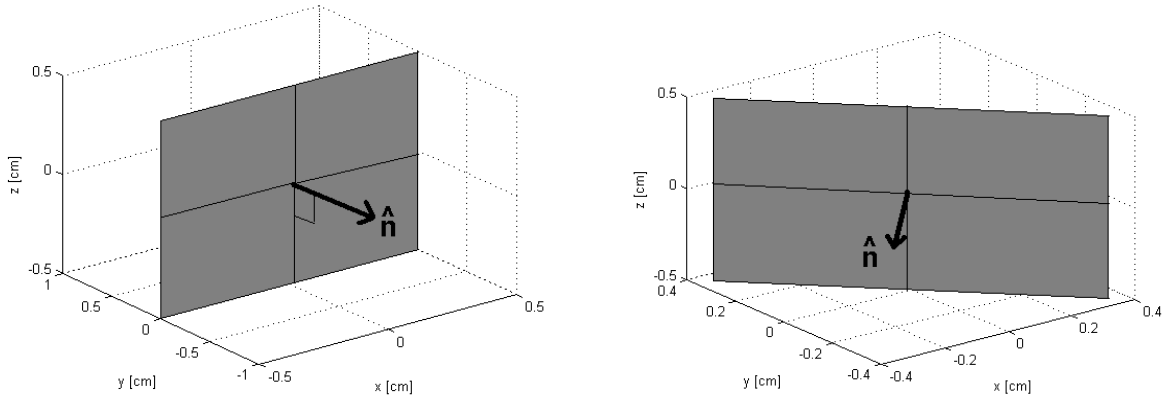

(a) (b)

Figure 15. Physical models of a single facet with respect to a global reference axis. The facets are directed with local normals, at (a) 0 deg rotation and (b) 45 deg rotation.

the most accurate geometric surface model provides the best results.

3.1.4.1 Cylindrical Surface Model.

As an example consider a cylinder viewed by our imaging system with projected pixel areas mapped onto the surface that are projected from the focal plane array. In Figure 16, each neighboring projected pixels in a row has a different incident and reflected angle, calculated with respect to the local normal of an individual projected pixel. Moving up or down through the row of projected pixels gradually moves to a new out of plane angular change to the BRDF calculation. With the small angle approximation, that out of plane angular difference provides negligible change to BRDF. Further detail on the geometric calculation of the specific angles corresponding to each projected pixel is provided in Appendix A. While, simple shapes can only provide an approximate geometry, ultimately an accurate human geometry provides the best surface representation.

www.manaraa.com

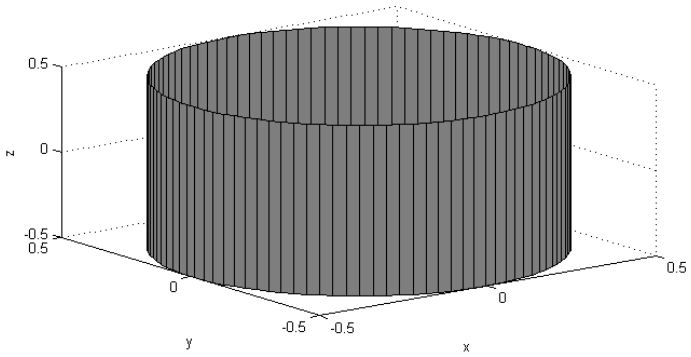

Figure 16. A cylinder with facets mapped out on its surface, projected from the focal plane array of our imaging system. Each facet has a local normal used for transforming the global incident illumination angle, into a local angle used in the calculation for skin reflectance.

3.2 Subsurface Reflectance

Subsurface reflectance is the diffuse component of the combined reflectance model, i.e., Equation (2.3.3). In [28], and reviewed in the Chapter 2, a nine layer Kubelka-Munk model characterizes diffuse reflectance from the subsurface, based on normally incident light. The subsurface contribution to reflectance is modified to consider light incident at angles off normal for wavelengths used in skin detection.

3.2.1 Normal Illuminated Reflectance Measurement.

An ASD FieldSpec3® radiometer collects combined spectral reflectance from the surface and subsurface of skin [1]. The probe with active source is pressed against the skin during measurement so the light is normally incident. Figure 17 is a measurement of Type I/II and Type V/VI skin from the field radiometer used for modeling.

3.2.2 Subsurface Reflectance Model Fitting.

The Type I/II and Type V/VI skin measurements in Figure 17 represent the extreme difference in skin types that we model. With the skin spectra from Figure 17,

www.manaraa.com

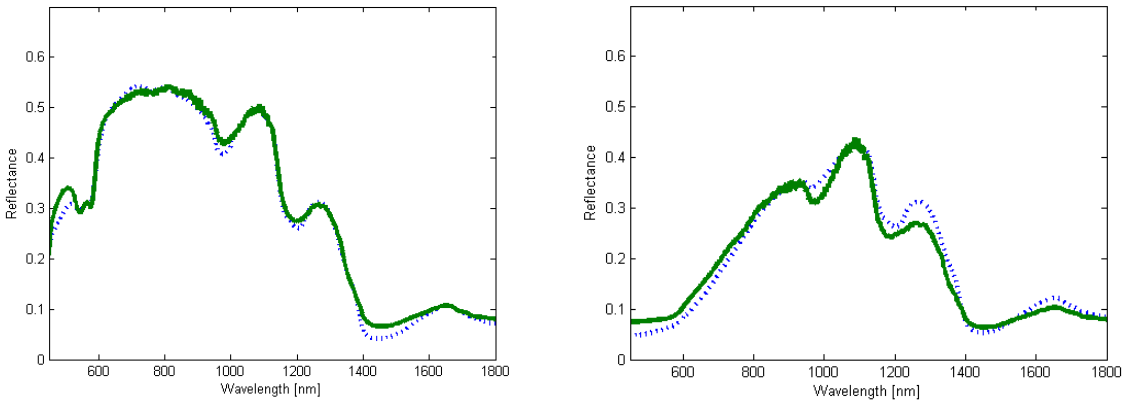

(a) (b)

Figure 17. Spectral reflectance from normally incident illumination of (a) Type I/II and (b) Type V/VI skin from [28]. The measured spectra (blue) is collected with the radiometer and modeled spectra (green) is fitted useing Kubelka-Munk.

the fitting parameters are found for the Kubelka-Munk model in Section 2.4.2. The measured spectrum is a sum of surface and subsurface components. The surface component is established in Chapter 2, for the case of normal incident light using the Fresnel Equation (2.2.4). The subsurface component is calculated from the Kubelka-Munk model with parameters fit to match the combined reflectance of Figure 17. With the Root Mean Square Error (RMSE) of Equation (2.4.14), a measure of difference between the measured and modeled data, we change the fitting parameters until we minimize RMSE. Applying the error function for all combinations of the variable parameters is computationally intensive. In [28], a database of radiometer collected data from subjects of different skin types was created, and a range of the parameter values was established that best represented a standard person for different skin types. In Table 2, the fit parameter values are shown for the Type I/II and Type V/VI skin spectra of Figure 17. A similar fitting is performed with the same method for any person.

www.manaraa.com

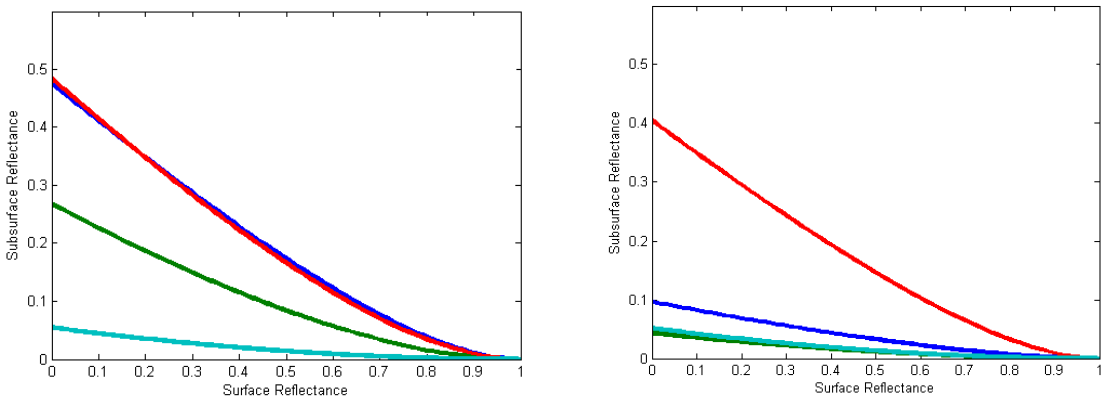

(a) (b)

Figure 18. Subsurface reflectance as a function of surface reflectance modeled with Kubelka-Munk for (a) Type I/II and (b) Type V/VI skin. The data represents wavelength regions of 544nm (green), 633nm (dark blue), 1080nm (red), and 1580nm (light blue).

3.2.3 Subsurface Angular Dependence.

With physical parameters fit to our specific subjects, a model now exists for normal incident illumination. Due to the conservation of energy, as front surface reflectance increases, the amount of flux transmitted into the first layer. Front surface reflectance (R_0) is calculated as Schlick reflectance ($\rho_{Schlick}$) from Equation (2.2.7), with the value subtracted from 1 to find the transmittance (T_0). As the incident angle changes for a specified projected pixel, a new front surface reflectance is calculated, thereby introducing angular dependence on the subsurface component of the BRDF model. With the established fitting parameters for the normally incident light in the

Table 2. Kubelka-Munk fitting parameters for our Type I/II and Type V/VI skin measurements.

Parameter	TypeI/II	Type V/VI
Melanosome %	3.5	40
Blood Level amount	0.9	1.1
Oxygenation %	50	18
Subcutaneous Scale	0.46	0.72

www.manaraa.com

previous subsection, the Kubelka-Munk model is run while varying R_0 from 0.04 to 1. In Figure 18, ρ_d is plotted as a function of R_0 for the Type I/II and Type V/VI skin spectra of Figure 17. A polynomial fitting is performed for each of the four wavelengths so that the Kubelka-Munk model does not need to be rerun for each projected pixel in a model of a particular person.

3.3 Surface Reflectance

Surface reflectance observed by the detector is the specular component of the combined reflectance model, i.e., Equation (2.3.4). In [28], the lambertian assumption was used to approximate skin as a diffuse surface in order to simplify the model for combined reflectance. We introduce a method to replace the lambertian assumption with a more representative model that accounts for the dependency of combined reflectance on source and detector angular locations. BRDF is the tool that characterizes a medium with those angular dependencies to generate a more accurate model. While there are many BRDF models that have been created for specific applications, we focus on a Gaussian microfacet model due to a similiar application in the simulation tool discussed later. The BRDFs for the visible wavelengths are measured directly with a commercial system, limitations force the BRDF's for the NIR wavelengths to be derived from image measurements.

3.3.1 BRDF ELM.

When working with surfaces defined with a BRDF, reflectance may change with source and detector configuration. While prior skin detection work focussed on source and camera positions normal to the sample surface, the work that follows focuses on off normal measurement and modeling. The DHR value for the reference Spectralon® is an adequate diffuse reflectance value to use in ELM while normal to the surface,

www.manaraa.com

but it breaks down as you move the source off normal. While Spectralon® is often considered a standard diffuse material, it has been shown in [7] that it gets increasingly more specular as the illumination incident angle moves off normal (see Appendix B for Spectralon® BRDF). By substituting BRDF from Equation (3.1.4) in for reflectance in the ELM Equations 2.5.5 and 2.5.6, the constant associated with the camera solid angle is lumped into the $a(\lambda)$ parameter to create the following form for ELM:

$$L_e(\theta_i, \theta_r, \Delta\phi, \lambda) = a(\lambda) \cdot f_{BRDF}(\theta_i, \theta_r, \Delta\phi, \lambda) + b(\lambda), \tag{3.3.1}$$

$$a(\lambda) = \frac{L_2(\lambda) - L_1(\lambda)}{f_{BRDF,2}(\theta_i, \theta_r, \Delta\phi, \lambda) - f_{BRDF,1}(\theta_i, \theta_r, \Delta\phi, \lambda)}, \tag{3.3.2}$$

$$b(\lambda) = \frac{L_1(\lambda) \cdot f_{BRDF,2}(\theta_i, \theta_r, \Delta\phi, \lambda) - L_2(\lambda) \cdot f_{BRDF,1}(\theta_i, \theta_r, \Delta\phi, \lambda)}{f_{BRDF,2}(\theta_i, \theta_r, \Delta\phi, \lambda) - f_{BRDF,1}(\theta_i, \theta_r, \Delta\phi, \lambda)}, \tag{3.3.3}$$

where $f_{BRDF,1}$ and $f_{BRDF,2}$ are the BRDF of our light and dark reference panels.

3.3.2 BRDF Measurement.

Our preferred approach to characterizing the BRDF of skin is with direct measurement. The Complete Angle Scatter Instrument (CASI®) is a commercially made scatterometer used to measure BRDF, seen in Figure 19. In our research, the CASI® system measures visible (VIS) wavelengths, but is not setup for our near-infrared (NIR) wavelengths. Since we cannot measure the NIR with the CASI®, a different approach is followed to fit BRDF parameters from images.

3.3.2.1 CASI® Scatterometer VIS Measurements.

The CASI® is a BRDF measurement device manufactured by Schmitt Measurement Systems. With a similar description to the Gonioreflectometer reviewed in Chapter 2, an armature holding the detector travels around the mounted sample gathering unpolarized data for a fixed incident angle at a set wavelength. The method

www.manaraa.com

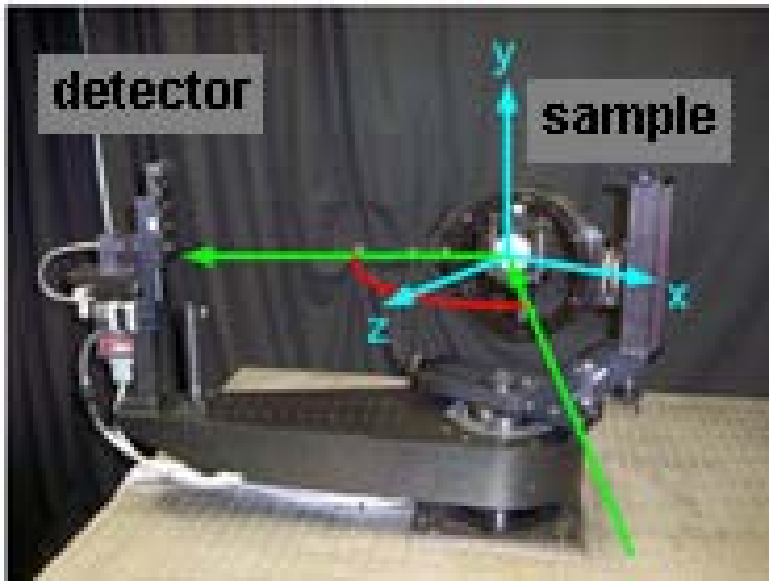

Figure 19. The CASI scatterometer featuring a detector and adjustable sample mount. The detector is attached to an arm that rotates around the sample. The green arrow indicates the path of light from a laser source, onto the sample which then reflects with the BRDF mapped out by the rotating detector.

for collection and plotted results of skin BRDF is presented.

The BRDF measurements are collected with the CASI® at our VIS wavelengths. The back of a Type I/II hand is placed at the sample location and in-plane BRDF is collected for the set incident angles of 0, 30, and 60 degrees. The corresponding plots are shown in Figure 20 for both VIS wavelengths used in detection. The dip for the 0 deg incidence plot, is due to the detector blocking the source during those collections interupting detection for those few points. For the 30 degree incidence plot we see noise in the collection, which may have been caused by movement of the hand during the collection. Fitting to data with this type of noise may pull us from an accurate fitting, and so we move forward to fitting our BRDF model with the 0 and 60 degree plots in the next section. For the NIR wavelengths an image-based approach was applied shown in Appendix D. Due to technical difficulties related to non constant illumination and reference materials this method was not used. Without a direct

www.manaraa.com

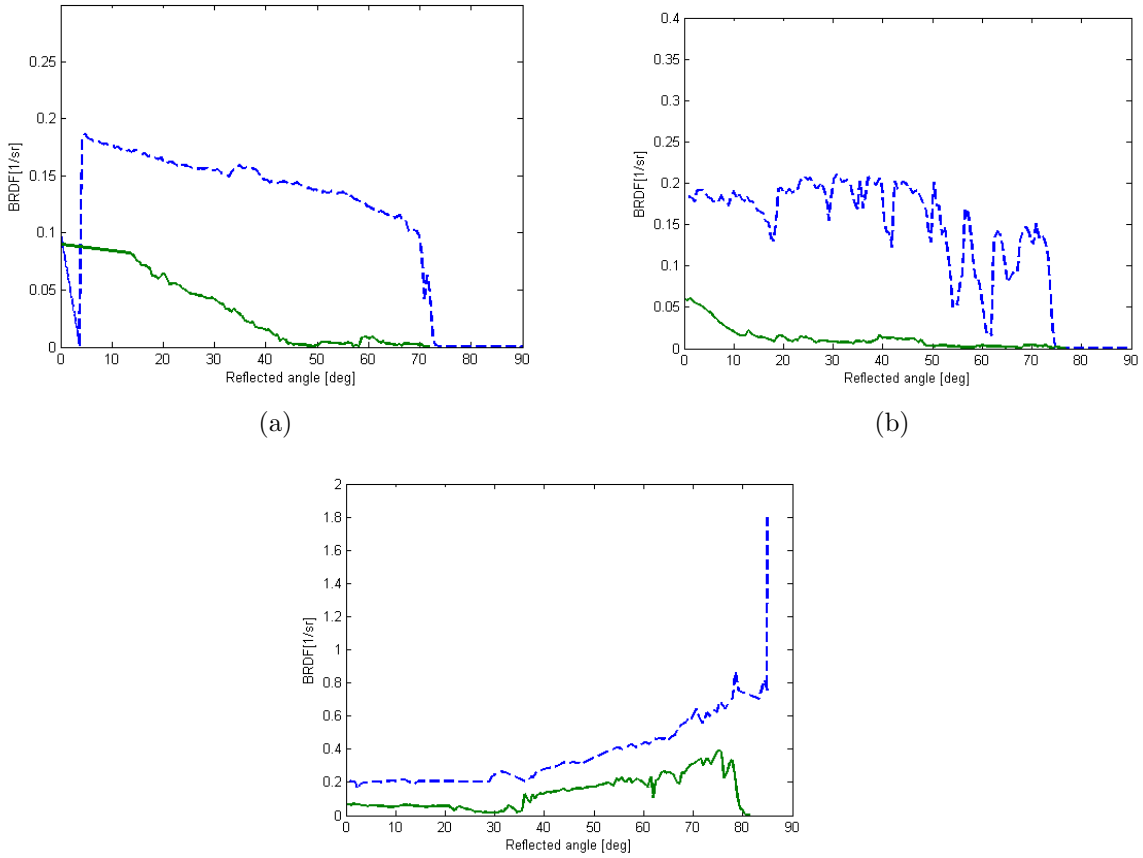

Figure 20. CASI® scatterometer measured BRDF at 544nm (green) and 633nm (blue) of Type I/II skin for incident angles of (a) 0 deg, (b) 30 deg, and (c) 60 deg.

BRDF measurement, the fitting parameters of our BRDF model in the NIR are fit directly to images collected with the AFIT SERG multispectral system in the next subsection.

3.3.3 Specular Reflection Model.

Since it would take too long to measure the BRDF of skin for every incident angle, including in and out of plane measurements, a model is fit to data collected for a few incident angles. We present our BRDF modeling of skin for the VIS wavelengths and then fit our BRDF model to images collected with the AFIT SERG system for the

www.manaraa.com

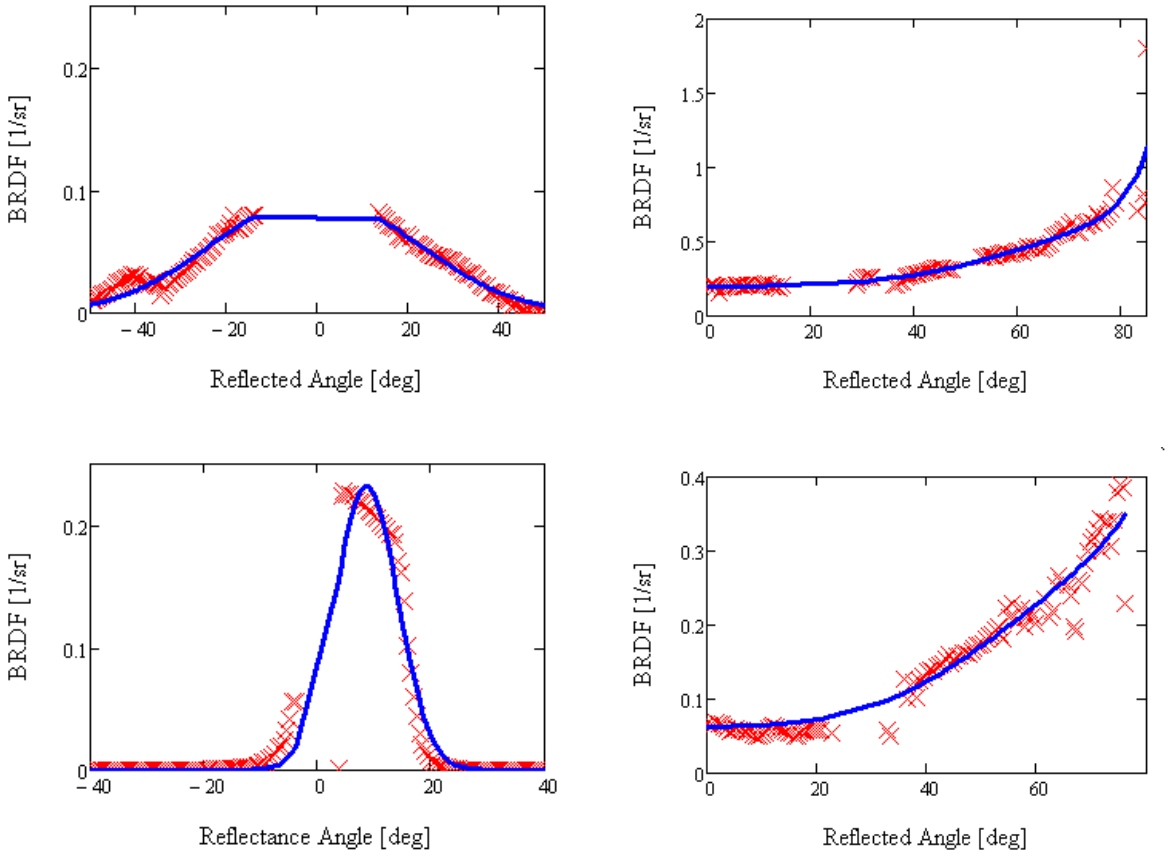

Figure 21. Type I/II skin measurements (red) and corresponding fitting of the microfacet BRDF model (blue) for (top) 544nm and (bottom) 633nm. The incident angles are set to (left) 0 deg and (right) 60 deg.

NIR wavelengths.

3.3.3.1 VIS BRDF Model Parameter Fitting.

The Gaussian nature of the specular lobe of media has led to the standard practice of using a Gaussian distribution for microfacet BRDF modeling. The microfacet model, while dependent on the interface indices, is also dependent on the orientation distribution of individual microfacets. The basis for generating an accurate model is by assigning a Gaussian distribution to the orientation, and fitting the parameters to measured data. The two fitting parameters for the Gaussian model are σ^2 and ρ_o.

www.manaraa.com

Figure 22. RGB image of the Type I/II subject, taken with the SERG multispectral detection system. The subject is in the center with reference panels on both sides to transform the scene into reflectance space.

With in-plane data collected, the two parameters are fit by minimizing the root mean square error (RMSE) between the model and measured values. In Figure 21, the model is fit to the CASI measured data for the 544nm and 633nm wavelength region. It was determined the best fitting for 544nm is a variance of 0.0313 and normal Schlick coeficient of 0.03 with an approximate RMSE of 1.8%. The best fitting for 633nm is a variance of 0.0292 and Schlick coefficient of 0.038 with an approximate RMSE of 8.2%. Applying Equation (2.2.4), we can back out the approximated spectral index at our detection wavelengths of 544nm ($n_2 = 1.42$) and 633nm ($n_2 = 1.42$).

3.3.3.2 NIR BRDF Model Parameter Fitting.

Without a direct way to measure the BRDF at the NIR wavelengths, the BRDF modeling parameters, σ^2 and ρ_o, are approximated with an image collected by the AFIT SERG detection system. In Figure 22, the RGB image from the AFIT SERG system of a Type I/II subject, illuminated 10 degrees off normal is shown. The image

www.manaraa.com

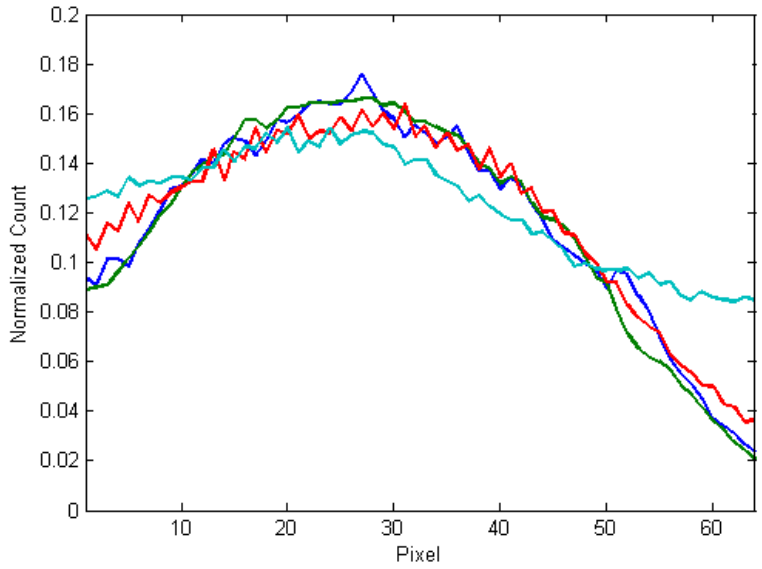

Figure 23. Normalized plot across the Type I/II subject forehead of Figure 22. The lines represent the different wavelengths for the AFIT SERG system of 544nm (dark blue) , 633nm (green), 1080nm (red), and 1580nm (light blue).

is then converted into reflectance space using the reference panels with ELM. Since the cameras have been aligned so that the images would correspond with each other for the detection algorithms, NDSI and NDGRI, a row of pixels across the forehead is selected for analysis. In Figure 23, the normalized spatial plot across the subject forehead is shown for each wavelength, where the normalized plot represents the change of reflectance in a common scale comparison. Since these lines represent the same surface geometry, it is our assumption that the difference in slope is a difference in BRDF affecting surface and subsurface reflectance observed by the detection system. Since, we have already fit the BRDF parameters for 544nm and 633nm, the incident (θ_i) and reflection (θ_r) angles that define the surface geometry for the j^{th} pixel in the row across the forehead are solved with the following equations:

$$\rho_j(544nm) = \rho_d(544nm, \theta_i) + \rho_s(544nm, \theta_i, \theta_r), \tag{3.3.4}$$

www.manaraa.com

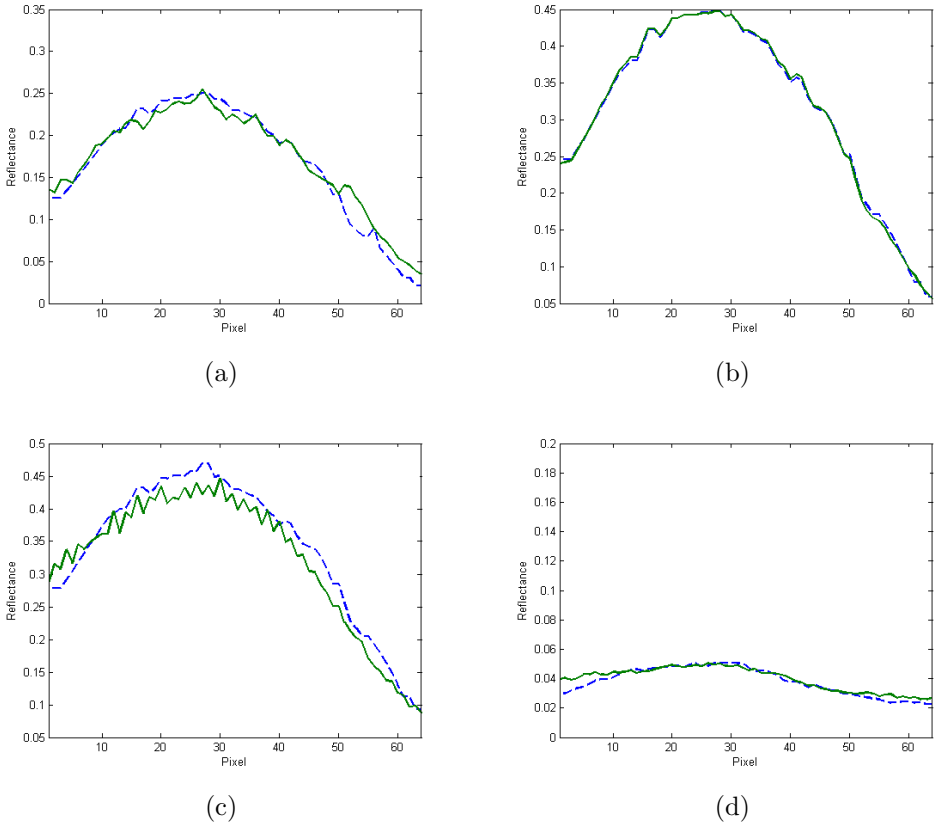

Figure 24. Modeled (blue) compared with measured (green) reflectance across the Type I/II subjects forehead from an image collected with the AFIT SERG multispectral camera system. The fitting is based on the surface geometry of the forehead. The plots correspond to wavelength regions of (a) 544nm, (b) 633nm, (c)1080nm, and (d) 1580nm.

$$\rho_j(633nm) = \rho_d(633nm, \theta_i) + \rho_s(633nm, \theta_i, \theta_r), \tag{3.3.5}$$

where ρ_d is observed subsurface reflectance modeled with Kubelka-Munk and ρ_s is observed surface reflectance modeled with the small angle BRDF Equation (3.1.4). The same surface geometry is run for 1080nm and 1580nm, in order to determine a best fitting for the BRDF parameters, with results from fit parameters seen in Figure 24. The best fitting for 1080nm is a variance of 0.0214 and normal Schlick coeficient of 0.045 with an approximate RMSE of 7.3%. The best fitting for 1580nm is a variance of 0.0146 and Schlick coefficient of 0.042 with an approximate RMSE of

www.manaraa.com

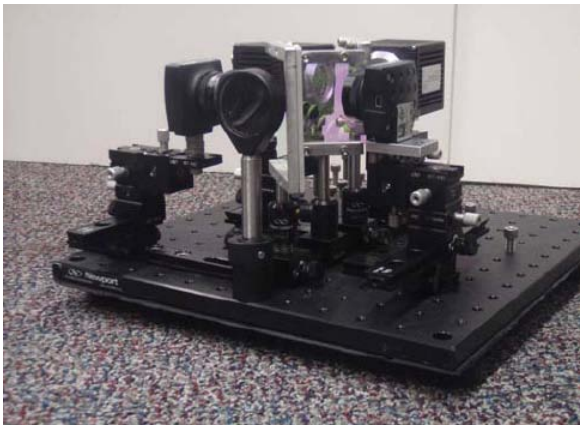

Figure 25. AFIT SERG multispectral detection system constructed in [30] and used for our experimental measurements. The system consists of an RGB camera and 2 Goodrich SIU cameras covering the range of 400-1700nm.

6.1%. Applying Equation (2.2.4), we can back out the approximated spectral index at our detection wavelengths of 1080nm ($n_2 = 1.54$) and 1580nm ($n_2 = 1.51$).

3.4 Experimental Scenario Measurement and Simulation

In order to verify our modeling results, images are collected with our AFIT SERG multispectral system, seen in Figure 25, for a controlled indoor experimental scenario. The study in [30] created the AFIT SERG multispectral system for skin detection, and compared collected data to results from the diffuse skin reflectance model in [28]. We perform a similar comparison of collected data, but we use modeling and simulation results accounting for combined reflectance that changes with the scene configuration.

In our experimental scenario, we limit the configuration changes to relocating the light source. Data is collected for illumination angles of 10, 30, 60 and 85 degrees from normal of the human subject. The detector is located normal to the subject and at a distance of 31 ft. The human subject is of Type I/II skin and remains in the same position for each illumination angle collected. Any movement of the

www.manaraa.com

camera or positioning of the human subject would introduce additional variables into the collection. While we discuss future work associated with variables to the human subject in Chapter 5, the next section introduces an environment to simulate scenarios with a variety of different configurations.

3.4.1 Scenario Simulation.

While basic shapes can represent parts of the human body, modeling with the actual form of a person provides the most accurate geometry. With the drive of the motion picture industry to constantly improve upon its animations and impress its audience, powerful software applications for rendering realistic scenes have been created. Blender® is a software package dedicated to providing realism to three dimensional animations [2]. Within Blender®, a virtual object is built or loaded in three dimensional space and rendered. We focus on simulating the indoor experimental scenario collected with the AFIT SERG multispectral system for the same configurations.

Within the Blender® interface, a model is built however the user chooses, but constructing an exact three dimensional replica of a specific person would be difficult. Blender® features a method to import Wavefront object files that contain a three dimensional model. With access to the three dimensional surface scanner from the 711th Human Performance Wing (AFRL/RHPA) at Wright-Patterson AFB, the human subject is digitized. In Figure 26, an illustration of the digitized subject is loaded into Blender® for simulations.

With the three dimensional subject loaded into Blender®, the surface reflectance characteristics are set to match that of skin. The Ward model settings within the Blender® BRDF toolbox allow us to set the two Gaussian parameters we fit from our BRDF measurements. A rendering is done for each wavelength represented by

www.manaraa.com

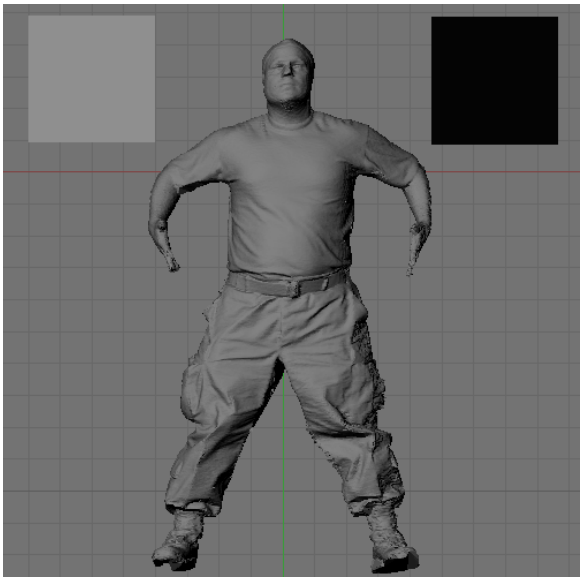

Figure 26. The digitized three dimensional human subject located between two reference pannels in Blender®. The panels are assigned lambertian reflectance values of 0.97 for the light colored panel and 0.03 for the dark colored panel. The human subject is assigned reflectance characteristics with the toolset of diffuse and specular shaders.

its own Gaussian parameters.

In the Blender® environment, detector and source characteristics are defined to be similar to those in the experimental scenario. In Figure 27, multiple camera and light source locations are illustrated and two reference panels are placed on the side of the scanned subject, similar to the measurements. All objects, including the digitized subject, can be repositioned anywhere in the virtual environment for future scenarios.

The output to the simulated scene is a rendered image in digital space that describes a pixel with an intensity value. The two panels are defined in Blender® as diffuse surfaces with different reflectance values of 0.97 and 0.03. While the scene is illuminated, these panels act as reference materials for performing ELM. Applying ELM to the reference panels of known diffuse reflectance creates a method for converting the entire image from digital space to reflectance space. A simple example is demonstrated in Appendix C with a diffuse object in place of the BRDF-defined person.

www.manaraa.com

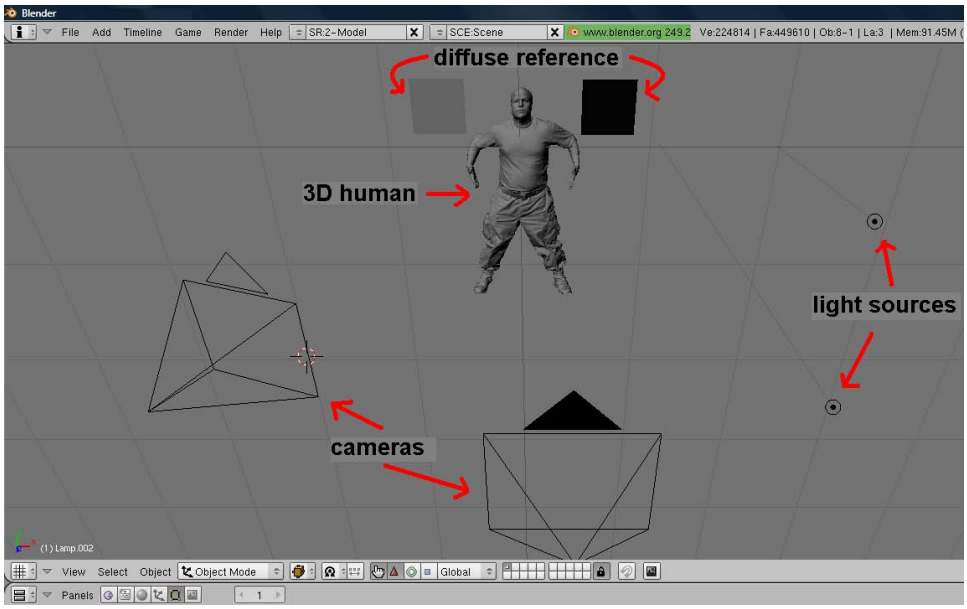

Figure 27. Blender® interface with 2 cameras and 2 light sources, demonstrating that each can be placed anywhere in the three dimensional space. The human subject and reference materials are the in-scene objects that are rendered.

3.5 Summary

In Chapter 3, BRDF models were fit for the wavelengths used in detection. A method described integration of the BRDF model into the existing diffuse reflectance model. In the next chapter, results to the surface models are compared with measured data from the AFIT SERG multispectral system.

www.manaraa.com

4. Results and Analysis

In Chapter 4, our experimental measurement and human surface modeling results are presented. The effect of off normal angular illumination on the rules-based detector is shown. Finally, a metric is used for the correlation between measured and modeled results.

In Chapter 3, we introduced the dependencies of the BRDF model, illustrated in Figure 28. Skin front surface reflectance calculated with Fresnel equations in Figure 2, demonstrates that for illumination angles from 0 to near 60 degrees, the front surface reflectance of skin is approximately 0.04. This low variation for these angles motivated the Lambertion assumption for front surface reflectance in the existing diffuse model [28]. However, for illumination angles greater than 60 degrees, the front surface reflectance increases and is more of a distribution, thereby motivating us to shift away from the lambertian skin assumtion. While specularity affects some pixels with a large increase in reflectance when viewing into the specular lobe, other pixels will have a large decrease in reflectance when viewing outside the specular lobe. Figure 28 illustrates that the location we view into the BRDF has a major impact on apparent reflectance. We show the effect in resulting rules-based detector scatter plots. With BRDF modeling, a method now exists to simulate many different scenarios in order to determine adjustable boundary conditions for the rules-based detector, dependent on the scene configuration.

4.1 Measurements Results

Images from the Air Force Institute of Technology (AFIT) Sensors Exploitation Research Group (SERG) multispectral system are presented, demontrating off normal illumination effects on apparent reflectance and the rule based detector. The resulting

www.manaraa.com

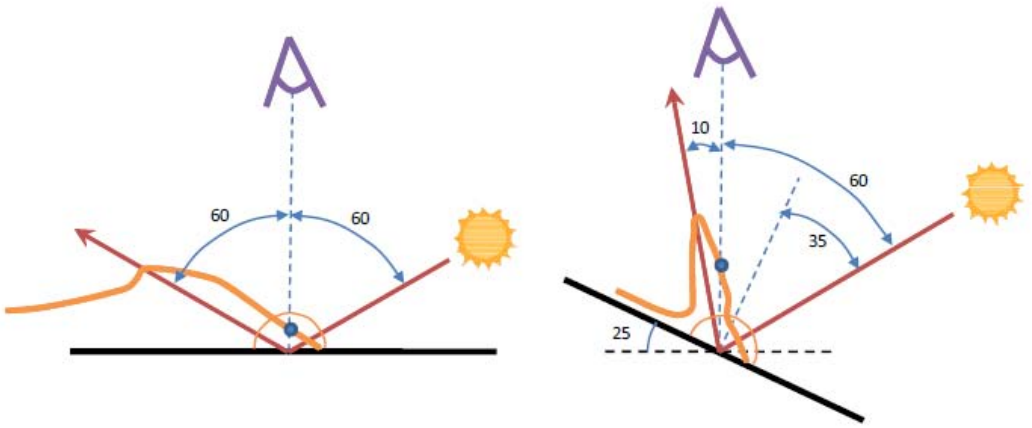

Figure 28. Diagram from [19], demonstrating the effect we characterize in the human skin results. There are two facet in the diagram, the left one is normal to the observer and the right one is rotated 25 degrees towards the illumination source. The facet BRDF drawn with the thick orange line, changes as a function of incident angle affecting reflectance seen by the observer. The dashed blue line goes from the observer to the facet and the blue dot intersects the applicable point on the BRDF curve.

Table 3. Directional Hemispheric Reflectance Values for our light and dark Spectralon Reference Panels.

Wavelength	White Panel	Dark Panel
$544nm$	0.989	0.075
$633nm$	0.990	0.079
$1080nm$	0.992	0.104
$1580nm$	0.988	0.133

histograms serves as a comparison to modeled data.

4.1.1 Measurement Uncertainty Analysis.

When measuring reflectance from off-normal illumination, our reference materials exhibit some form of specular reflection changing with wavelength, since they are not perfectly diffuse (seen in Appendix B). With our reference Spectralon® panels, Labsphere provided us with normal illuminated DHR values for wavelengths in the visible (VIS) to near-infrared (NIR). The DHR values for our wavelengths of interest are listed in Table 3. Since we do not have the BRDF of our panels, we do not know

www.manaraa.com

how the apparent reflectance of our reference materials changes with illumination angle. Since we use the panels in a linear regression for the Empirical Line Method (ELM), uncertainty in the panel reflectance at off normal illumination angles introduces uncertainty in our computed reflectance. Our simulated Blender® environment uses ideal reference materials; therefore, the uncertainty is a cause of difference between the measured, simulated, and true reflectances. To calculate the uncertainty, we use the BRDF Spectralon® plots (Appendix B) at 633nm for VIS wavelengths and 3390nm as the closest available for the NIR wavelengths. In Chapter 3, with the small angle assumption, we relate apparent reflectance to BRDF through a solid angle that remains constant for our measurements. Therefore, we relate a change in BRDF to a change in apparent reflectance of the pannels. The largest error across the BRDF plots shown in Appendix B is seen at 75 deg incident illumination for both wavelengths. We calculate the change in BRDF from 0 to 75 deg illumination angle for a camera position of 0 deg, as a comparable error to our DHR values. Therefore, using the normal incident DHR values at illumination angles off normal introduces a maximum estimated error of 4.1% in the VIS and 7.4% in the NIR.

4.1.2 Experimental Scenario Measurement.

In Figure 29, each image for the scenario shown configured as Figure 30, representing each wavelength for detection of the Type I/II subject, is mapped into reflectance space. The longer wavelength colors (i.e., red) correspond to high reflectance and shorter wavelength colors (i.e., blue) correspond to low reflectance following the color scale. Since the source is only 10 degrees off normal for these images, a majority of the pixels are viewing skin that have a local incident illumination angle under 60 degrees. However, locations of high specular reflection directed into the camera contribute to the high reflectance values and locations of high specular reflection directed away

www.manaraa.com

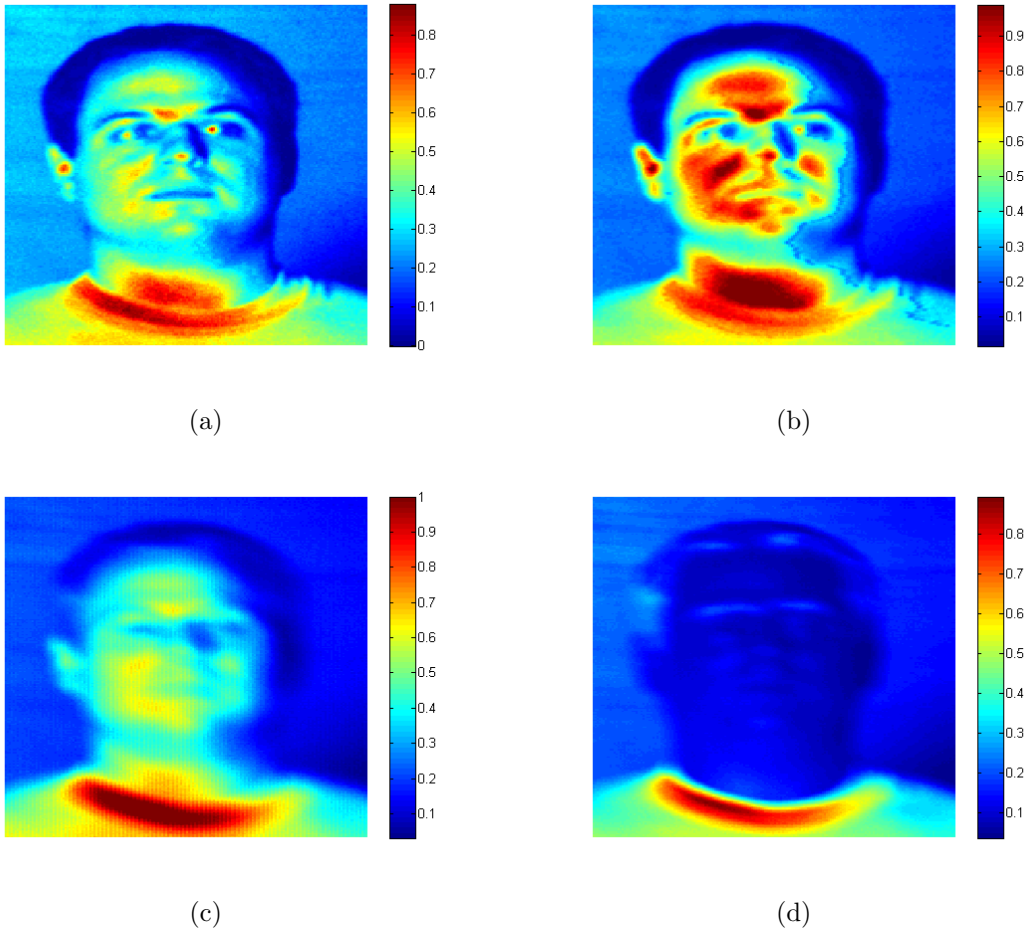

Figure 29. Image taken with the AFIT SERG multispectral system, seperated into wavelength regions of (a) 544nm, (b) 633nm, (c) 1080nm, and (d) 1580nm. The scenario has the camera normal to the subject and the light source 10 deg off normal. The images are in reflectance space differentiated in value by the corresponding color scale.

from the camera contribute to lower reflectance values.

To demonstrate the effect specular reflection has on our measurements, images are also aquired with the AFIT SERG multispectral system for illumination angles of 30, 60, and 85 degrees off normal. As the illumination angle moves further off normal to the subject, shown in Figure 31 for 60 degrees illumination, pixel reflectance values spread out above and below the normal incident diffuse value. The effect is explained by the notion that as we are close to normal illumination, seen with the 10 degree

www.manaraa.com

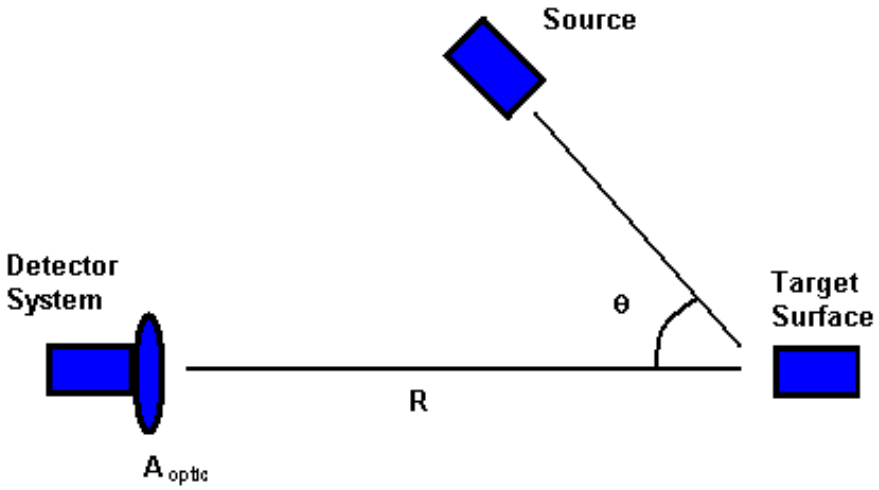

Figure 30. Diagram of our experimental scenario for our AFIT SERG multispectral system viewing a Type I/II peson. The source is located θ degrees from normal to the person.

images, a majority of the light is incident on skin under local illumination of 60 degrees for a front surface reflectance of 0.04 resulting in an apparent reflectance similar to the radiometer measured value for those pixels. For those conditions, subsurface reflectance is the driver for observed reflectance. As we move the angular illumination towards 85 degrees, more of those pixels are viewing reflectance from skin local illuminated greater than 60 degrees. According to Fresnel, the rate of change on reflectance for local incident angles greater than 60 degrees is steep. The sharp slope combined with the random surface geometry on the subject results in values across the reflectance scale for large incident angles. The side of the subject with the illumination source exhibits an increase in reflectance since the specular reflection is directed to the camera. Since the illumination on the side of the face without the light source is not constant, reflectance is lowered. This is an artifact of the measurement that is characterized.

www.manaraa.com

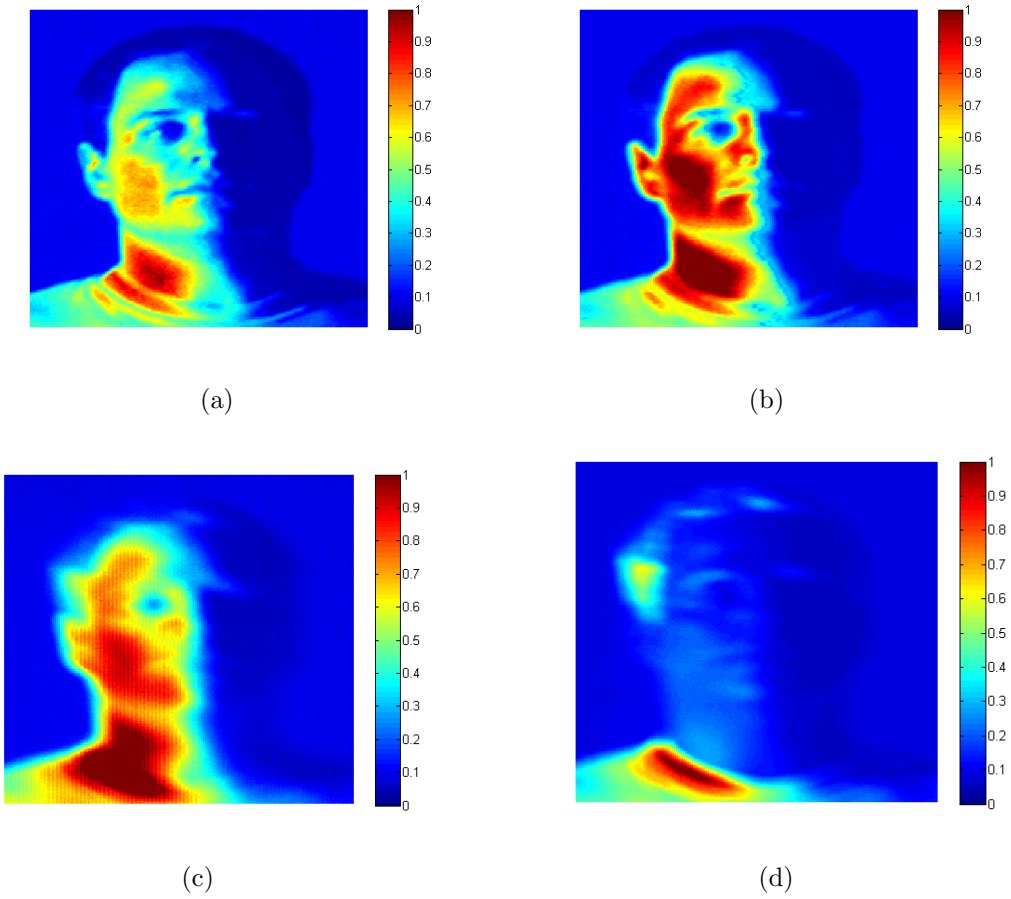

Figure 31. Images captured with the AFIT SERG multispectral system illuminated 60 degrees off normal to the subject and converted into reflectance space for wavelengths of (a) 544nm, (b) 633nm, (c) 1080nm, and (d) 1580nm.

The measurements are used to find NDGRI and NDSI values for each pixel resulting in a scatterplot for the rule based detector in Figure 32. While all dots plotted are skin pixels the blue dots represent pixels detected as skin, while the green dots are rejected and are considered as other objects. The plots show how pixels fall outside the boundary for skin detection as the illumination incident angle increases. At 85 degree illumination, nearly every pixel is rejected, since they fall outside the boundary. A trend in the shift of pixels, for the respective wavelength, from the diffuse value measured with the radiometer to high or low reflectance values depends

www.manaraa.com

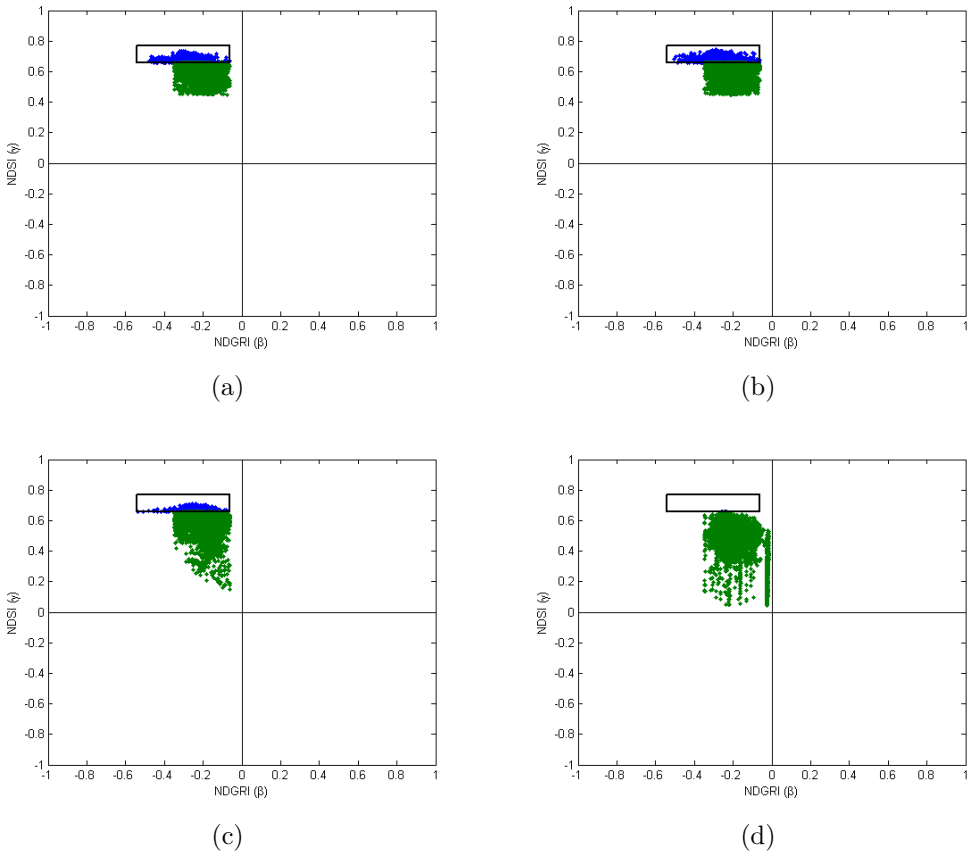

Figure 32. Rules-based scatterplot of the data collected with the AFIT SERG system for illumination angles of (a) 10 deg, (b) 30 deg, (c) 60 deg, and (d) 85 deg. The blue points indicate skin that meets the rule based criteria; the green points are pixels that are skin, but do not meet the critera for the detector based on boundary set from the diffuse model.

on scene configuration. Accurate characterization of the changing pixels is an indicator for adjusting the rules-based boundary conditions. Figure 33 is a histogram for the distribution of pixels in the first quadrant of the scatterplot and are used for a correlation comparison in the next section.

4.2 Modeling Results

Reflectance modeling of surfaces viewed from the perspective of the AFIT SERG multispectral detection system is explored. The configuration used for our experi-

www.manaraa.com

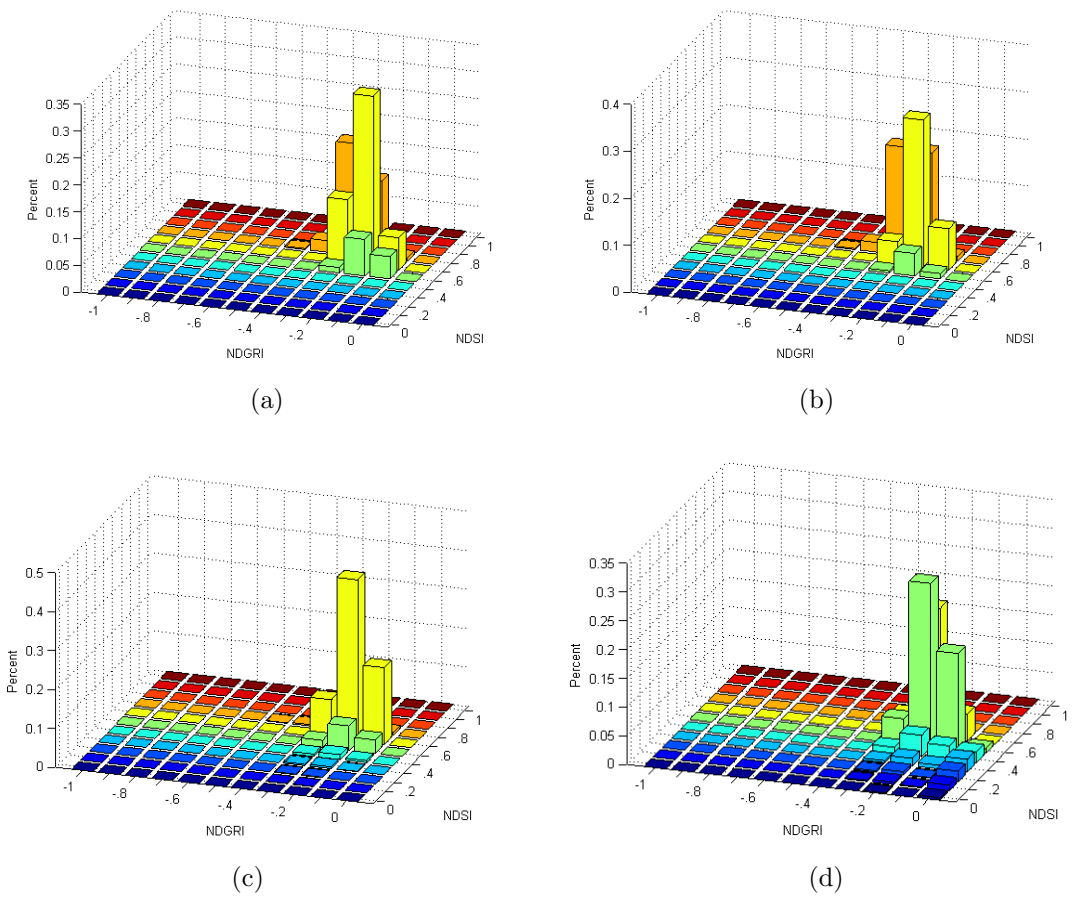

Figure 33. Histogram of the rules-based scatterplot of the data collected with the AFIT SERG system for illumination angles of (a) 10 deg, (b) 30 deg, (c) 60 deg, and (d) 85 deg. The graphic represents the distribution of pixels falling into a specific NDSI vs NSGRI bin.

mental measurements is used within the modeling environment for comparison.

4.2.1 Human Surface Simulation.

Simulation with the most accurate three dimensional model is our approach to estimating apparent reflectance. In order to simulate the experimental scenario, Blender® is utilized with the three dimensional person. In this section we give simulated results to the experimental scenarios with the digitized human subject.

The subsurface spectral reflectance that is driven by Kubelka-Munk modeling is

www.manaraa.com

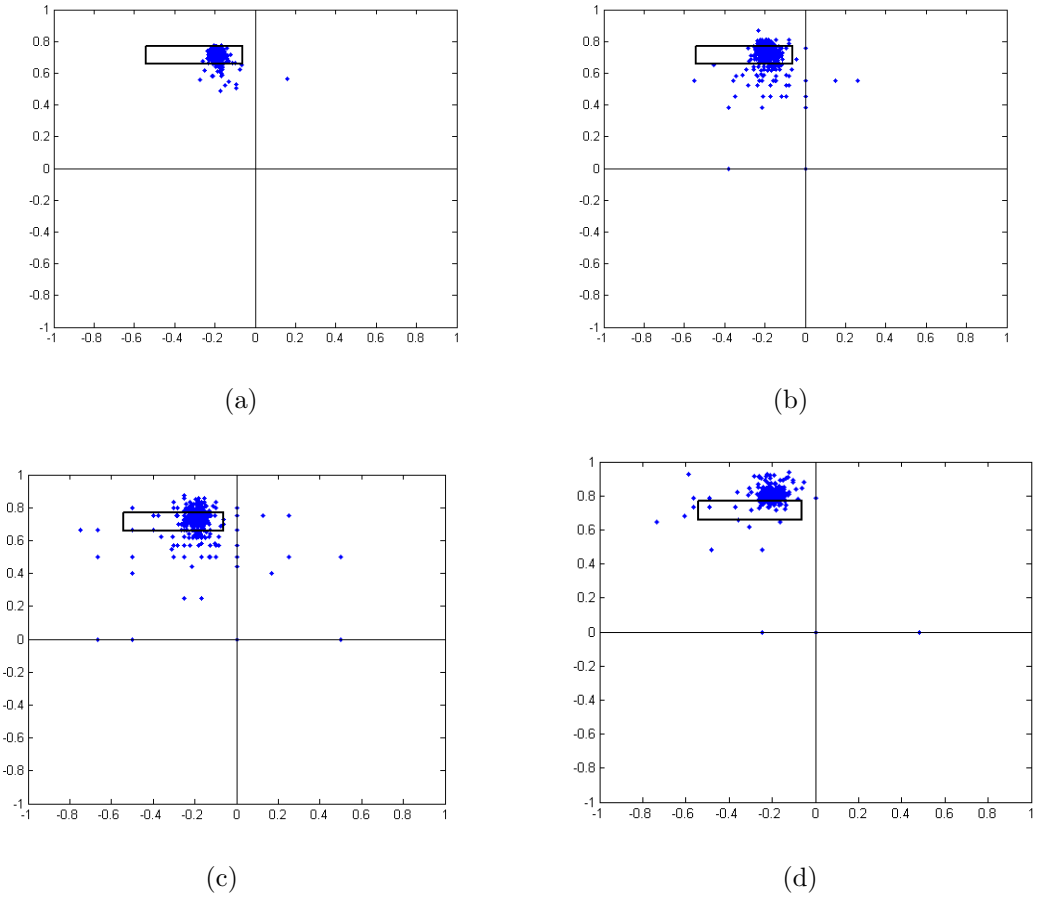

Figure 34. Results of diffuse only skin modeling for incident illumination angles of (a) 10 deg, (b) 30 deg, (c) 60 deg, and (d) 85 deg.

not included in the Blender® package. Objects illuminated within Blender® can have an underlying diffuse reflectance that is adjustable. The diffuse reflectance is set to the radiometer measured reflectance value unique for the human subject Type I/II skin and for the respective wavelength rendered. The software has a front surface proportionality correcting the diffuse value with a change in local illumination angle. The BRDF parameters used for surface roughness $\sigma^2(\lambda)$ and normal illuminated reflectance $\rho_o(\lambda)$ are both spectral terms adjusted with a change in wavelength.

A plot of our rules based detector on data modeled with a diffuse only component is presented in Figure 34. The results show that our boundary conditions are

www.manaraa.com

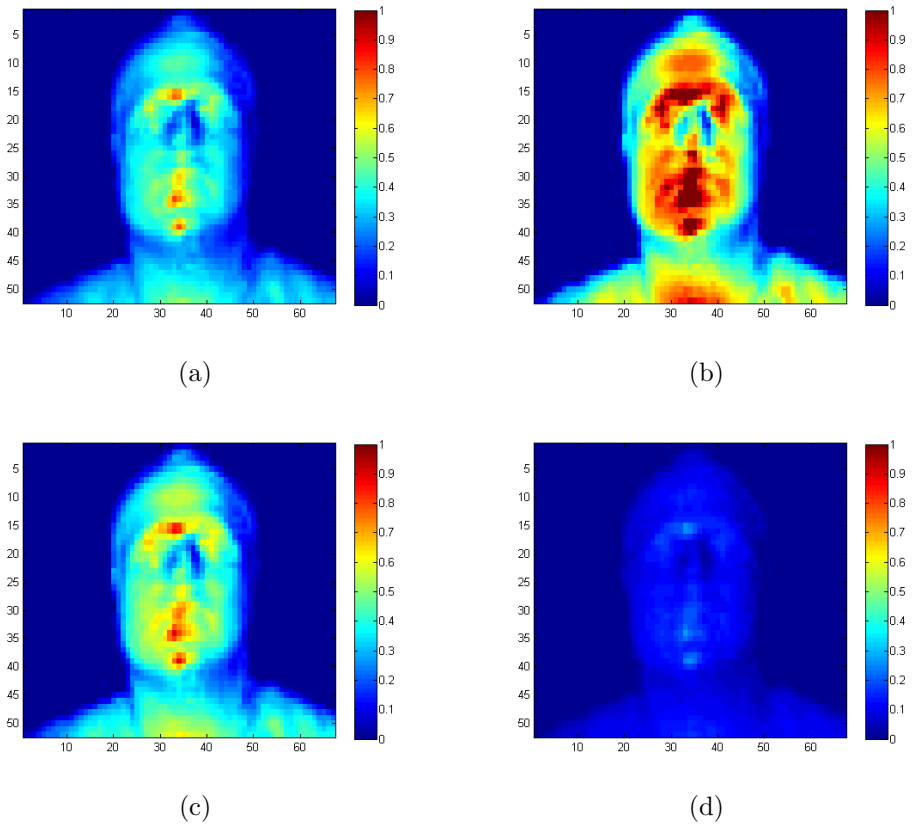

(a) (b) (c) (d)

Figure 35. Blender rendered images converted to reflectance space modeling (a) 544nm, (b) 633nm, (c) 1080nm, and (d) 1580nm. The modeling scenario has the camera normal to the human subject and source 10 degrees off normal.

a good indicator for skin when only considering the diffuse reflectance component. Since NDGRI is a measure of difference between two wavelengths, the change is front surface reflectance proportionally changes both 544nm and 633nm reflectance while preserving the difference between them. For NDSI our 1580nm wavelength has low reflectance and the change is front surface reflectance is not proportional with 1080nm, resulting in a shift of the cluster within the scatterplot.

The scenario where the source is 10 degrees off normal to the human subject is rendered with images shown in Figure 35. It is evident that variations across the face are related to the specular reflectance and they match well to the corresponding

www.manaraa.com

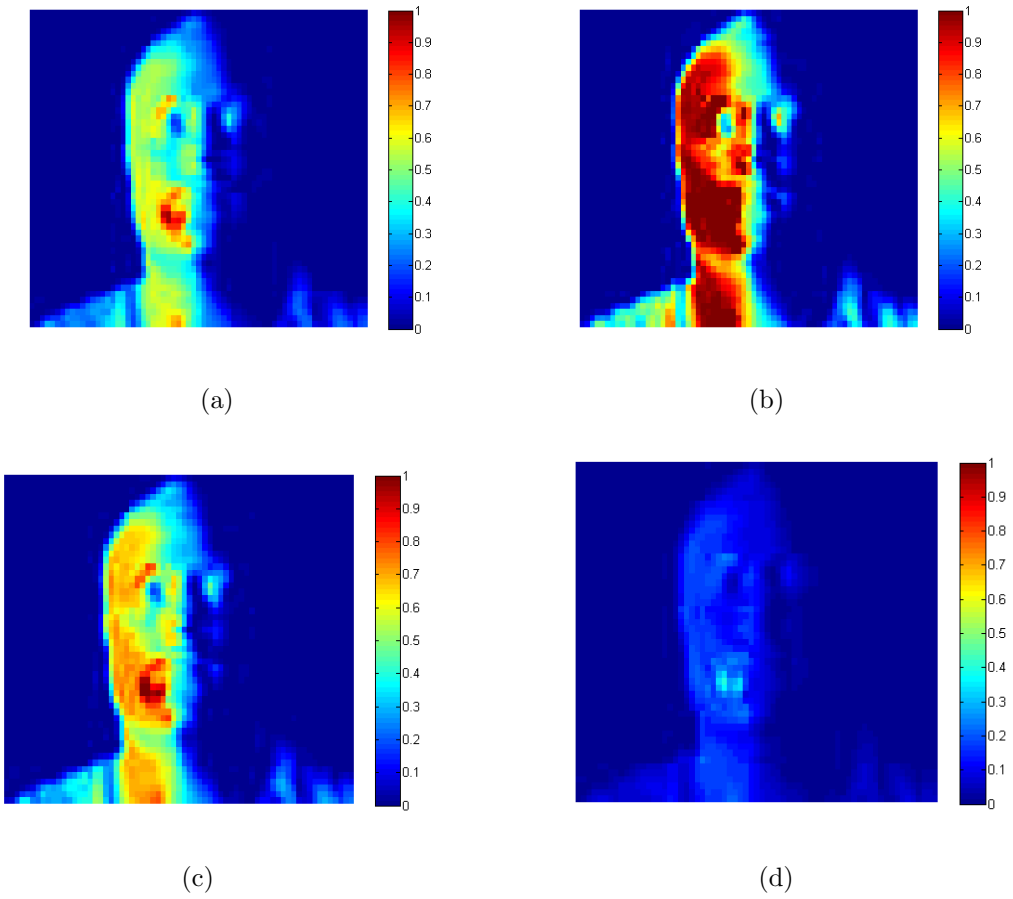

Figure 36. Rendered images for a scene configuration illuminated 60 degrees off normal to the subject and converted into reflectance space for wavelengths of (a) 544nm, (b) 633nm, (c) 1080nm, and (d) 1580nm.

measured images from Figure 29. The scenario where the source is 60 degrees off normal to the human subject is rendered with images shown in Figure 36. Within the 60 deg illuminated images the nonconstant illumination on the other side of the face is similiar to that of the measurements. Although nonconstant illumination is not ideal conditions for performing the emperical line method, a reduced apparent reflectance is shown to be similar to the measurements.

A metric for the measure of overlap between the modeling and measurement his-

www.manaraa.com

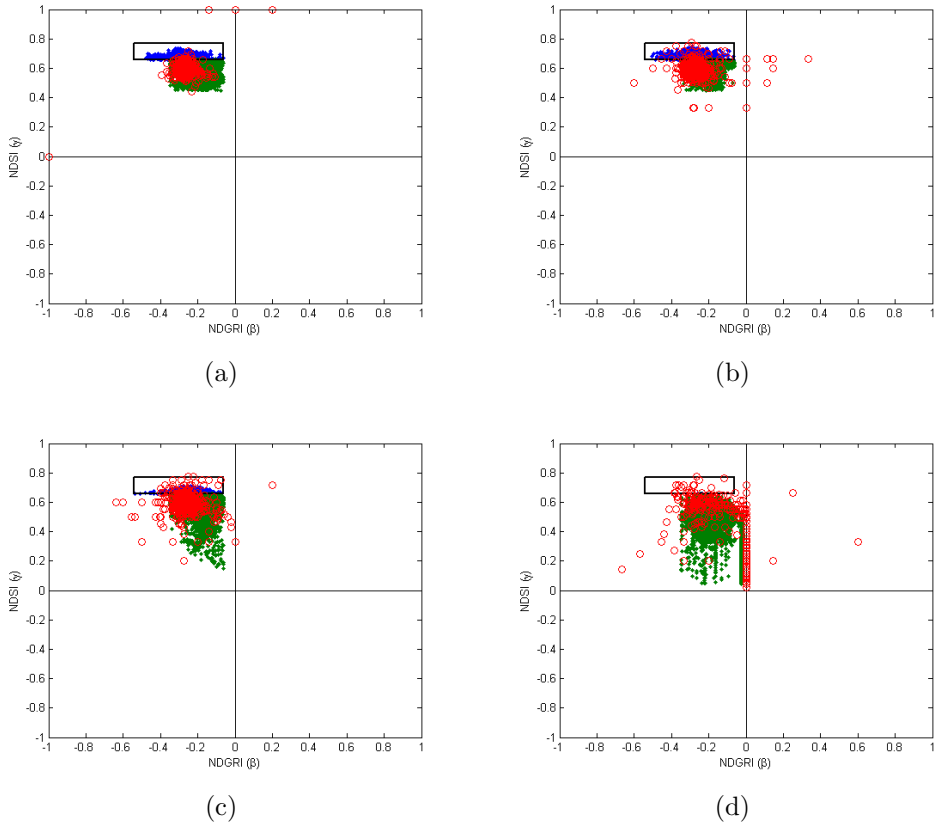

Figure 37. Rules-based scatterplot of the data collected with the AFIT SERG system and Blender simulated data, for illumination angles of (a) 10 deg, (b) 30 deg, (c) 60 deg, and (d) 85 deg. The blue points indicate skin that meets the rules-based criteria; the green points are skin pixels not meeting the critera for skin based on diffuse modeling. The red circles are blender simulated data. The rectangle is the boundary for skin pixels in the rules-based detector.

tograms is the Bhattacharyya coefficient (BC) calculated as:

$$BC = \sum_{i=1}^{n} \sqrt{p_i \cdot q_i}, \tag{4.2.1}$$

where p_i and q_i represent the percent of the cumulative number of pixels in the i^{th} bin for measured and modeled histograms. A BC closer to 1 indicates higher correlation in the data, where a BC closer to 0 indicates less correlation in the data. In Figure 37, the rules-based detector is applied to the Blender® data in red and plotted over

www.manaraa.com

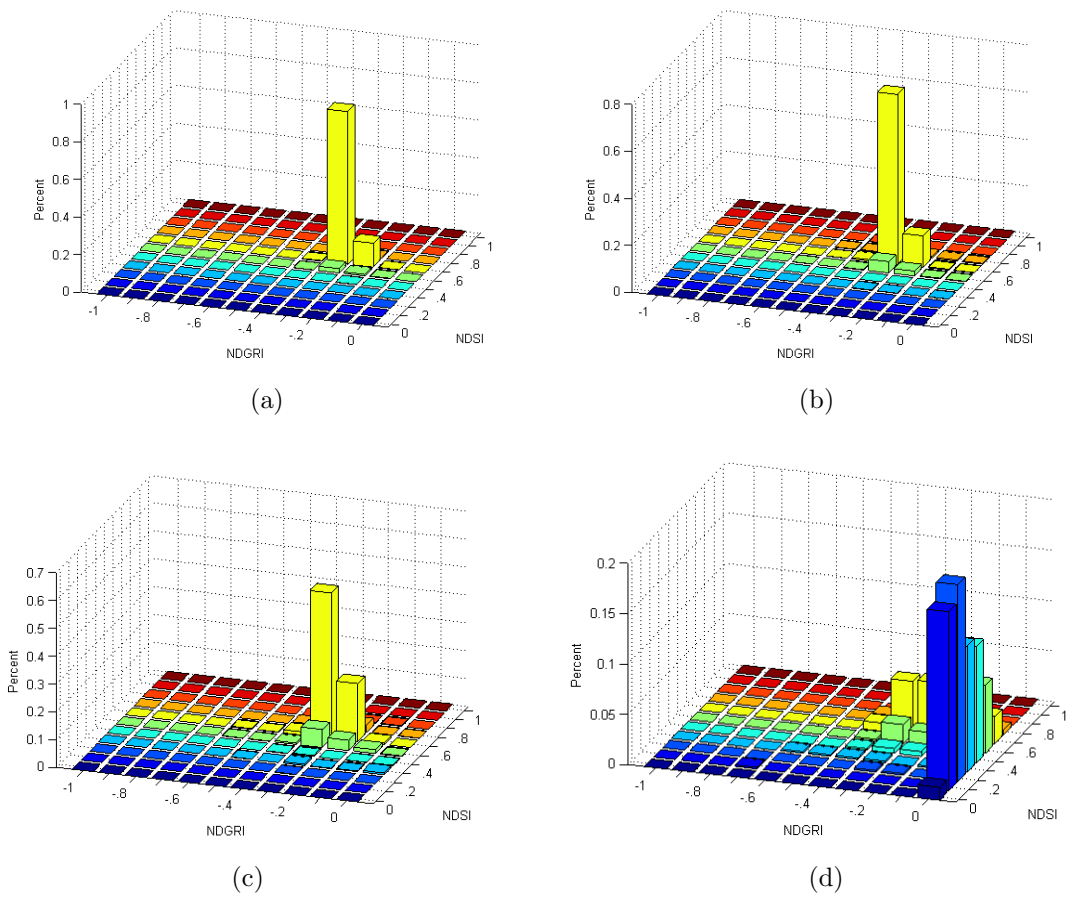

Figure 38. Histogram of the rules-based scatterplot of the blender modeled scenario with illumination angles of (a) 10 deg, (b) 30 deg, (c) 60 deg, and (d) 85 deg. The graphic represents the distribution of pixels falling into a specific NDSI vs NSGRI bin.

the scenario measured data points. The rendered data aligns favorably with the measured data from the scatterplot. When comparing the diffuse only model with the diffuse plus specular model, it is clear that an increase in specular reflectance provides the general shift in pixels out of the boundary region. It is evident that modeling with a diffuse plus specular model gives a better reflectance estimate than just the diffuse model alone. The added specular component allows us to estimate the shift in the cluster of pixels representing skin when applying the rules-based detector. The corresponding distribution of values for the rendered data scatterplot is shown

www.manaraa.com

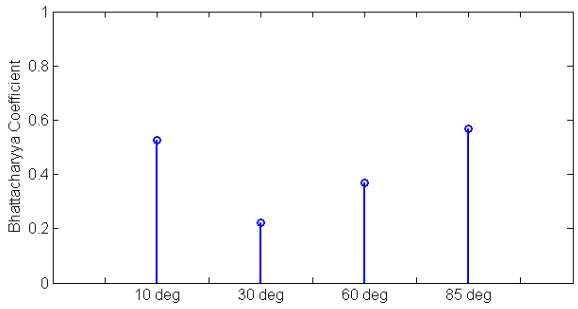

Figure 39. Bhattacharyya coefficient of the 2 dimensional histograms representing the correlation between measured and modeled distributions of NDSI vs NDGRI at illumination angles of 10, 30, 60, and 85 degrees.

in Figure 38. The correlation between the measured and modeled distributions of Figure 33 and Figure 38 with the BC for each of our illumination angles is shown in Figure 39. The correlation is best at 10 and 85 degree illumination, but there is room for improvement. Additional refinement of the BRDF modeling parameters at 1080nm and 1580nm and characterization of our reference panels are future work described in the next section.

4.3 Summary

The results presented in Chapter 4 are from an evolving model that originated from previous research for the subsurface reflectance in [28], with added work from our current research on surface reflectance. Modeling of an experimental scenario was accomplished to estimate apparent surface reflectance as a function of scene configuration.

www.manaraa.com

5. Conclusion

In Chapter 5 our summary and conclusions are given of the work accomplished on skin Bidirectional Reflectance Distribution Function (BRDF) characterization and reflectance modeling. Recommendations for future work related to BRDF measurement at the near infrared (NIR) wavelengths and application of the model to improve on human detection are discussed.

Our research goals were to characterize the BRDF of human skin for the wavelengths used in human detection and incorporate specular reflection into the existing diffuse reflectance model. The first goal was met with a combination of direct measurement and extraction from a test scenario with the Air Force Institute of Technology (AFIT) Sensors Exploitation Research Group (SERG) multispectral system. Since the commercial CASI® system was setup for measurement at 544nm and 633nm, the unpolarized in-plane BRDF of human skin was characterized for incident angles of 0, 30, and 60 degrees. A method was developed with an image-based setup to characterize BRDF at 633nm with the intent to move into measureing 1080nm and 1580nm, but a reference BRDF of the labsphere panels at those wavelengths is needed. Instead, the NIR wavelengths were fit from a measurement scenario of the AFIT SERG multispectral system. The Schlick normal reflectance and variance parameters were found which provide a reflectance distribution with the microfacet model for any incident angle between 0 and 90 degrees. The second goal with human surface modeling in the Blender® environment. Modeling was performed for illumination angles similar to an experimental scenario with a calculated comparison. We now discuss future work needed in this area and conclusions to our accomplishments.

www.manaraa.com

5.1 Future Work

5.1.1 Dismount Detection.

While the goal of our work was to improve on the skin reflectance model, the eventual application is to better detect people. In Chapter 2, the Normalized Difference Skin Index (NDSI) and Normalized Difference Green Red Index (NDGRI) were introduced as calculations for the rules-based detector. Shown in our research was a reflectance model of skin that includes a specular and diffuse components, thereby realizing a more accurate representation of normalized difference (ND) algorithms:

$$ND = \frac{[\rho_d(\lambda_1, \theta_i) + \rho_s(\lambda_1, \theta_i, \theta_d)] - [\rho_d(\lambda_2, \theta_i) + \rho_s(\lambda_2, \theta_i, \theta_d)]}{[\rho_d(\lambda_1, \theta_i) + \rho_s(\lambda_1, \theta_i, \theta_d)] + [\rho_d(\lambda_2, \theta_i) + \rho_s(\lambda_2, \theta_i, \theta_d)]} \tag{5.1.1}$$

where λ_1 is 1080nm and λ_2 is 1580nm for NDSI, or λ_1 is 633nm and λ_2 is 544nm for NDGRI, θ_i is the global incident angle, and θ_d is the global viewing angle. If the detection system is viewing into the specular lobe, a large difference in value for the two wavelengths is less likely and the resulting value is driven closer to zero since the denominator will be much larger. Future work may be interested in setting the threshold for detection with modeling estimations based on source and detector angular locations. With the simulation tool, the digitized human subject is setup in any orientation to a source and camera in three dimensional space to estimate apparent reflectance for the rules-based detector.

5.1.2 Skin Shade Variation.

While observing a person with the human eye, it is clear that some people are visibly dark shaded and others are light shaded. The modeling in [28] revealed that the subsurface component drives the effect of this skin type. Meanwhile, the front surface component was shown to add or subtract to this effect based on surface

www.manaraa.com

geometry. While the subsurface component is matched to a specific person, the surface component was shown to change as the geometry of the individual changes. Since the head and neck are most commonly exposed and are similiarly shaped for people, these areas were the focus of modeling and simulation of this research. Adjusting the diffuse value in the model for the respective skin type allows us to estimate reflectance values for any person. Additional measurements and modeling with darker shader subjects is needed to validate the model for use with diferent shaded subjects.

5.1.3 Sources of uncertainty.

While including a BRDF model showed favorable modeling results, additional work is needed to increase accuracy. The BRDF models fit at 1080nm and 1580nm were approximated and based on image measurements, but an accurate BRDF measurement is needed to refine the model at those wavelengths. Additionally, due to an unknown amount of specularity from our reference Spectralon pannels, some error is introdused into our experimental measurements. Characterization of our panels at our detection wavelengths is needed to make that correction. In additional, with better panel characterization we can move to scenarios that incorporates different camera positions. As of now, moving the camera position into a specular lobe will add additional uncertainty to our measurements.

5.2 Conclusion

As was shown in our modeling results, the rendered images that included a specular modeling component correlated more favorably with the similar scenario measured with our multispectral system than just the diffuse value alone. The rendered images run through the rules-based detector proved to be an adequate indicator for skin pixels. We increased fidelity in our method of skin reflectance estimation from a single

www.manaraa.com

diffuse value representing each of the wavelengths used in detection to a distribution of values across the human subject.

www.manaraa.com

Appendix A. Facet Geometry

To determine estimated reflectance through the combined skin reflectance model, a method was developed to work with representative shape surfaces for the human body. The surfaces are facetized by assuming a small angle approximation for the projected field of view for a single pixle element of the imageing system. In this appendix the global illumination incident angle is transformed to local angles for the surfaces demonstrated in this research.

For a single flat facet in Figure 15 whose local normal aligns with the global reference normal, the following symbols representing the physical configuration are defined as follows:

- The range (R) is the distance from the source area to the detector.
- Area of the optic (A_d) for calculating the solid angle of the detector.
- Facet area (A) is the projected detector element following Equation (2.2.3).
- Reflected angle (θ_d) is the angular difference of the detector from the reference axis.
- Incident angle (θ_i) is the angular difference of the source from the reference axis.

Three cases were demonstrated in this thesis for modeling which included viewing outside the specular lobe which resulted in diffuse only component observed and viewing directly into the specular lobe with (θ_i) equals (θ_d) in the corresponding reflection quadrant.

The cylindrical geometry in Figure 16 is realized with the equation of a circle with estimated radius of the appendage. Most of the symbols are similar to the single facet geometry, but the global angles are transformed into local angles for each facet with

www.manaraa.com

the following equations:

$$\theta_{rot} = \arctan(\frac{y}{x})$$
$$\theta_{i,local} = \theta_{i,global} - \theta_{rot}$$
$$\theta_{r,local} = \theta_{rot} - tan^{-1}(\frac{R + r - x}{y})$$

where the symbols are defined as:

- Rotation angle (θ_{rot}) is the angular rotation between the global reference axis and the local facet normal.
- Local reflection angle ($\theta_{r,local}$) and incident angle ($\theta_{i,local}$) calculated for each projected facet.
- Coordinates on the cylinder represented by x and y.
- The radius of the circle is r.

www.manaraa.com

Appendix B. Spectralon BRDF

The labsphere spectralon panels have been used for all calibration in this research. In [7], spectralon BRDF was characterized with the CASI system. The resulting plots are shown in Figure 40 for 633 and 3390nm wavelengths at 4 different incident angles.

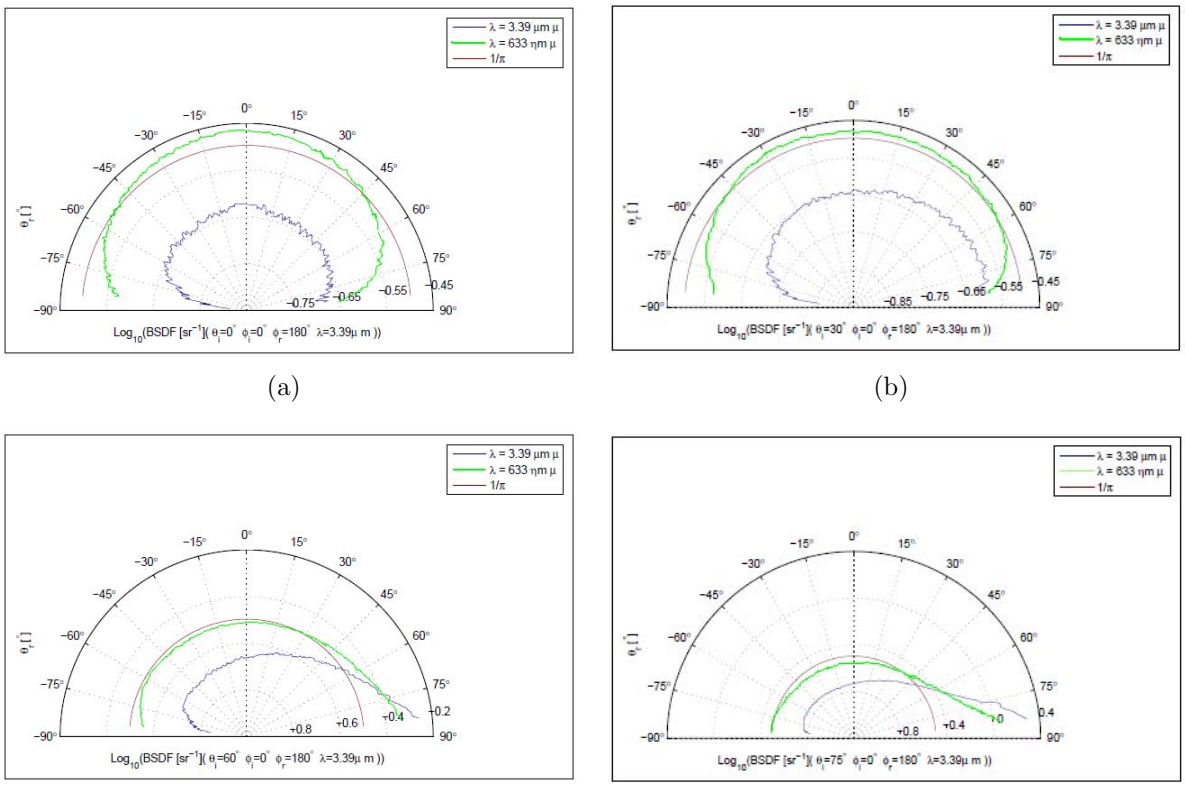

Figure 40. Measured BRDF of Labsphere spectralon from [7] using the CASI® system at 633nm and 3390nm for incident angles of (a) 0 degrees, (b) 30 degrees, (c) 60 degrees and (d) 75 degrees.

www.manaraa.com

Appendix C. Scene Simulation

This appendix demonstrates a method for useing Blender software to simulate a remote sensing scenario by testing a simple case with three diffuse panels. The outer two panels are defined as the reference panels with reflectances of 0.97 and 0.02 respectively. In this scenario a diffuse panel with reflectance of 0.4 is placed in the center, but any arbitrarily shaped surface with BRDF characterization can take its place. For this test the source and camera are placed normal to the surface, but these objects can be placed anywhere in the hemisphere above the panels for future experiments.

In Figure 41 a layout of this configuration is displayed where the outer squares represent the camera field of view and the dot above the center panel represent the light source. The blender interface allows the user to define the material diffuse and specular characteristics. For the specular shader there are several predefined BRDF models in Blender with adjustable parameters to set for the desired response.

With a rendered image of the scene it can now be treated as any picture when applying analysis techniques is matlab. So, ELM is calculated using the two reference panels to convert the rendered image from digital space into reflectance space. Figure 43 is a histogram of the rendered image after converted into reflectance space. What it shows is that the values assigned in blender to the three panels are mapped in reflectance space with an error of $\pm$ 0.02.

www.manaraa.com

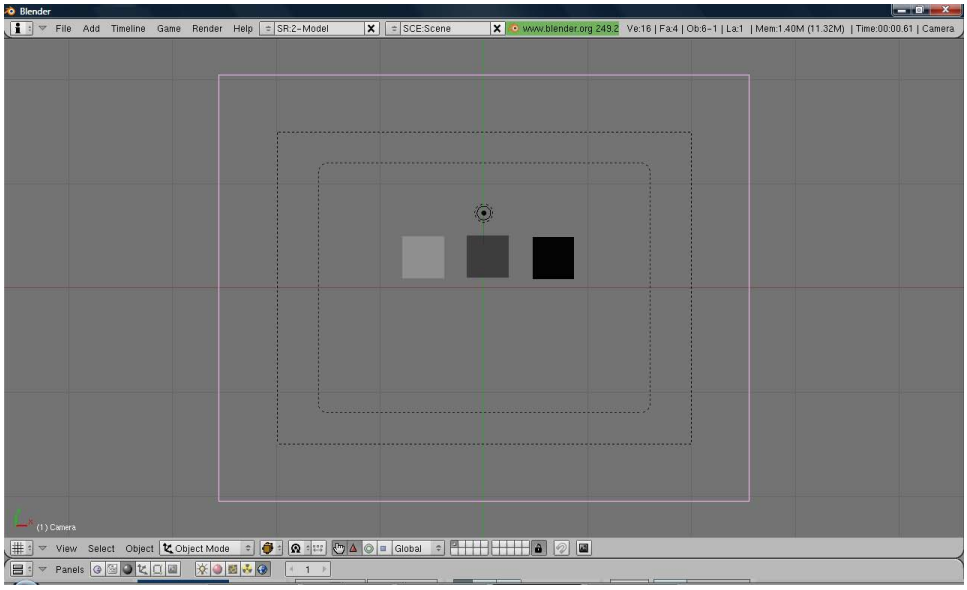

Figure 41. Blender interface of three reference panels assigned varying diffuse reflectance characteristics.

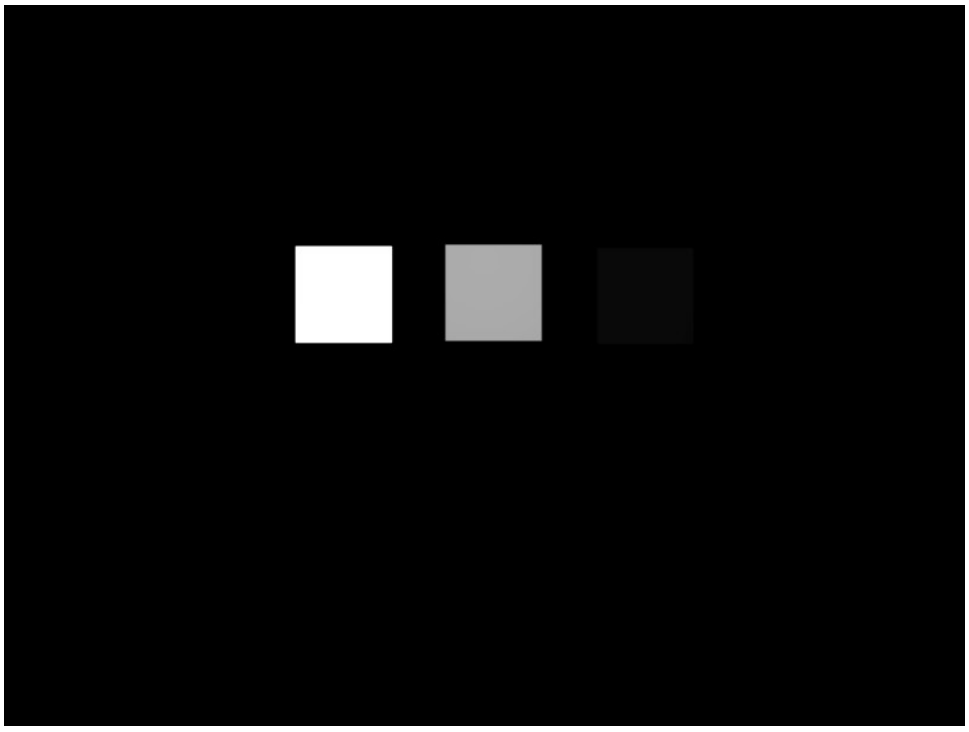

Figure 42. Rendered image of three reference panels wheresource and detector are normal to the surface.

www.manaraa.com

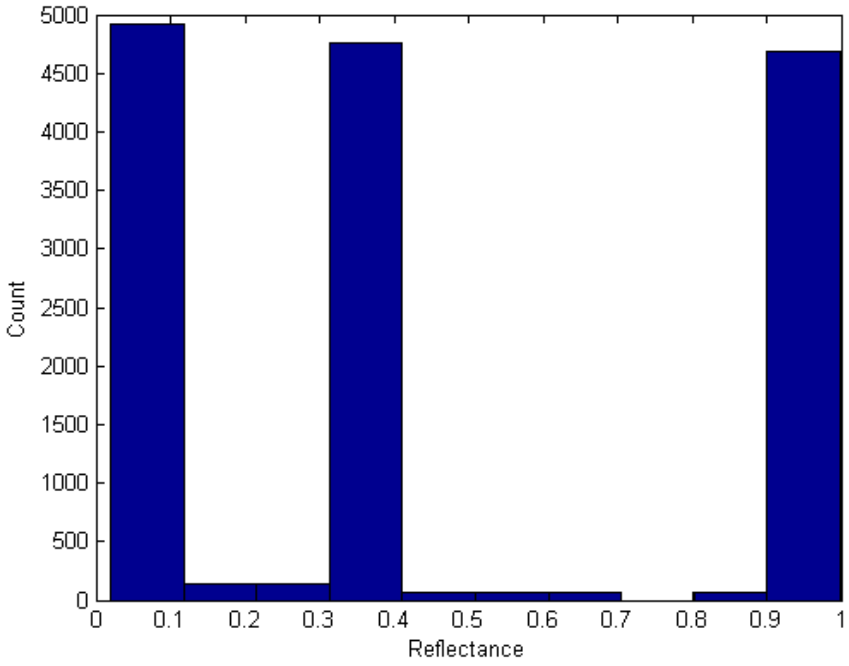

Figure 43. Histogram of reflectance values from the simulated image after mapping from digital space into reflectance space with ELM.

www.manaraa.com

Appendix D. Image-Based Measurement

The limitation to our NIR wavelengths for the current setup of the CASI® system requires us to characterize BRDF at NIR wavelengths with an alternative method. In Chapter 2, some novel methods for an image-based BRDF design were described. Those concepts are the influence to an image-based method for characterizing in-plane BRDF for skin at our NIR wavelengths.

An image-based method with the Figure 14 configuration is our first approach to characterizing BRDF at the NIR wavelengths. The method configures the image-based system with the parameters listed in Table 4, to define the range from the sample to the detector, source and detector angles with respect to the sample normal, and optic area for the collection. The extended version of a Goodrich SIU camera is used covering 400nm to 1700nm. For the source, collimated light is directed to the sample location from an off-axis parabolic mirror (OAP). The OAP is an optical component that is a section of a full parabolic mirror with a focal point of 304.8 mm. When the incoming rays from the laser source diverge from the focal point of the OAP, they collimate upon contact with its surface at an expanded area. A snapshot of the system layout in Figure 44 shows these components with a Spectralon® panel at the sample location. The red dashed line is the path for light with arrows showing the direction.

The image data from the Goodrich camera is in the form of a digital number representing the intensity of radiation, originating from a laser source, reflecting from

Table 4. Image-Based Measurement System Parameters.

Parameter	Value	Units
A_{optic}	19.60	cm^2
R	64.0	cm
θ_s	0, 60	degrees
θ_d	10, 20, 30, 40, 50, 60, 70, 80	degrees

www.manaraa.com

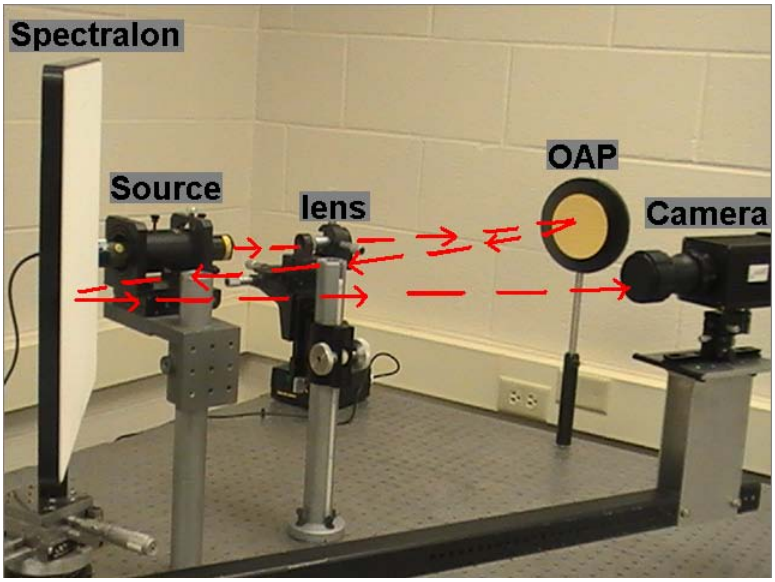

Figure 44. Setup of the image-based measurement system, showing the illumination path in red with arrows pointing the direction. The laser source is aligned so that the light would diverge from the lens, at the focal point of the OAP. The camera is attached to an arm for rotation around the sample. A Spectralon panel rotated 45 degrees from the incoming light is located at the sample location.

the hand and reaching the camera. All other lighting in the room is turned off during the collection. To transform the digital number into a BRDF value, we use the BRDF ELM with Equations (3.3.1), (3.3.2), and (3.3.3). Two Labsphere Spectralon® panels are the reference standard for the calculations. The BRDF of Spectralon® at 633nm, shown in Appendix B, was measured at AFIT in [7] and represents the reference BRDF used to find the ELM parameters.

In Figure 45, the image-based measurement of the Type I/II skin is compared along with the CASI measurement for 0 and 60 degrees. The image-based BRDF data follows the same trend in both plots but may differ from the CASI® data with an approximate RMSE of 9.4% at 0 degrees and 1.2% at 60 degrees. We attribute most error to the source, reference material, and camera angle corrections. First, the collimated light is variant across the illuminated hand due to corrosion on the OAP. The reference BRDF from [7] is used to represent the standard BRDF of our panels

www.manaraa.com

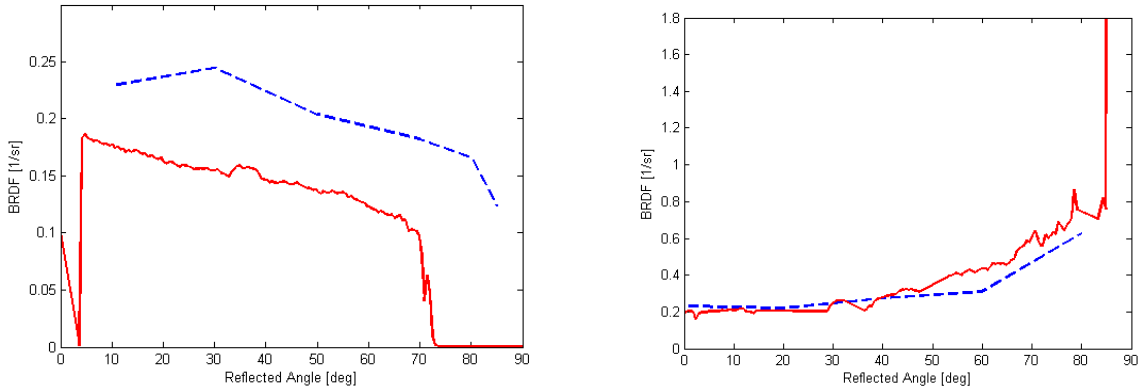

(a) (b)

Figure 45. The image-based BRDF measurements of Type I/II skin (blue) compared with the CASI® measurements (red). The illumination source is at 633nm with an incident angle of (a) 0 deg and (b) 60 deg.

which may be different. Finally, while the camera positions are set manually, this introduces a ±3 degree error with cosine correction for the increase in area viewed by an instantaneous pixel. Furthermore, since we are unable to characterize BRDF of our Spectralon® panels for the NIR wavelengths, the direct measurement approach is not used to characterize skin at our NIR wavelengths. The following recommendations are advised for improvement with the system. Characterize our reference panel BRDFs for all our wavelengths of interest. Improve the illuminating source to bring it closer to space invariant conditions. Automate the rotating arm collection system to increase angular accuracy.

www.manaraa.com

Bibliography

[1] "ASD FieldSpec 3". Website. URL*https://www.asdi.com/products/fieldspec-3*.

[2] "Blender". Website. *https://www.blender.org/*.

[3] "Digital Imaging and Remote Sensing Image Generation". Website. URL *https://www.dirsig.cis.rit.edu/*.

[4] "NASA". Website. *http://www.nasa.gov/topics/earth/features/obscure data.html*.

[5] "vrarchitect". Website. *http://www.vrarchitect.net/anu/cg/GlobalIllumination/BRDF.en.htmll*.

[6] B. Stevenson, W. Kendall A. Stocker W. Schaff D. Alexa J. Salvador M. Eismann K.Barnard, R. O'Connor and J. Kershenstein. "Design and performance of the Civil Air Patrol Archer hyperspectral processing system". *Algorithms and Technologies for Multispectral, Hyperspectral, and Ultraspectral Imagery XI*, 5806:731–742, June 2005.

[7] Balling, Bradley. *A Comparative Study of the Bidirectional Reflectance Distribution Function of Several Surfaces as A Mid-Wave Infrared Diffuse Reflectance Standard*. Master's thesis, Graduate School of Engineering, Air Force Institute of Technology(AETC), 2009.

[8] Brooks, Adam L. *Improved Multispectral Skin Detection and Its Application to Search Space Reduction For Dismount Detection Based on Histograms of Oriented Gradients*. Master's thesis, Graduate School of Engineering, Air Force Institute of Technology(AETC), 2010.

[9] Cheong, Prahl S.A., W. and Welch A.J. "A review of the optical properties of biological tissue". *IEEE Journal of Quantum Electronics*, 26(12):2166–2185, 1990.

[10] Connant, John A and Jr. Frank J Iannarilli. "Development of a combined bidirectional reflectance and directional emittance model for polarized modeling". *Polarization Analysis, Measurement, and Remote Sensing IV*, 4481(Proc. SPIE):206–215, 2002.

[11] Cook, R.L. and K.E. Torrance. "A reflectance model for computer graphics". *ACM Transactions on Graphics*, 1(1):7–24, 1982.

[12] Dana, Kang, J. and Jim Wang. "Device for convenient measurement of spatially varying bidirectional reflectance". *Optical Society of America*, 21(1):1–12, 2004.

[13] Dereniak, E.L and G.D. Boreman. *Infrared Detectors and Systems*. A Wiley-Interscience Publication, New York, NY, 1996.

www.manaraa.com

[14] Goldstein, E. Bruce. *Sensation and Perception*. Wadsworth Group, Pacific Grove, California, 2002.

[15] Gondec, J.S, G.W Meyer, and J.G Newman. "Wavelength Dependent Reflectance Functions". *1SIGGRAPH '94 Proceedings of the 21st annual conference on Computer graphics and interactive techniques*, 1–8. 1994.

[16] Hecht, Eugene. *Optics Fourth edition*. Addison Wesley Publication, San Francisco, CA, 2002.

[17] Henrik Jensen, Marc Levoy, Stephen Marschner and Pat Hanrahan. *A Practical Model for Subsurface Light Transport*. Technical report, Stanford University.

[18] Hornung, Matthew P. *Flexible Computing Architecture for Real Time Skin Detection*. Master's thesis, Graduate School of Engineering, Air Force Institute of Technology(AETC), 2010.

[19] Ientilucci, J. E. and Gartley M. *Impact of BRDF on Physics Based Modeling as Applied to Target Detection in Hyperspectral Imagery*. Technical report, Digital Imaging and Remote Sensing Laboratory, Rochester Institute of Technology.

[20] Jengo, C.M. and J. LaVeigne. "Sensor performance comparison of HyperSpecTIR instruments 1 and 2". *Proceedings IEEE Aerospace Conferen*, 3:1805. March 2004.

[21] J.R. Maxwell, S. Weiner D. Ladd, J. Beard and S. Ladd. *Bidirectional reflectance model validation and utilization*. Technical report, AFAL-TR-73-303 Environmental Research Institute of Michigan, 1973.

[22] Kendricks, Ronald F. Tuttle, Kimberly D. and Adam Fullenkamp. "An Inverse kinematic mathematical model using groebner basis theory for arm swing movement in the gait cycle". *submitted to the journal of Biometrics*, 2010.

[23] Krishnaswamy, A. and Baranoski. G. *A Study on Skin Optics*. Technical report, University of Waterloo, Canada, 2004.

[24] Lambert, J.H. *Photometria sive de mensura et grabibus luminis, colorum et umbrae*. Technical report, Augsberg, Germany, 1760.

[25] Li, Foo S.-C. Torrance K. E., H. and S. H. Westin. "Automated three-axis gonioreflectometer for computer graphics applications". *Optical Engineering*, 45(4):1–11, 2006.

[26] Marschner, Stephen. *Inverse Rendering for Computer Graphics*. Ph.D. thesis, Cornell University, 1998.

[27] Matts, P.J. Dykes, P.J. and R. Marks. "The distribution of melanin in skin determined in vivo". *British Journal of Dermatology*, 156(4):620–628, April 2007.

www.manaraa.com

[28] Nunez, Abel S. *A Physical Model of Human Skin and Its Application for Search and Rescue*. Ph.D. thesis, Graduate School of Engineering, Air Force Institute of Technology(AETC), Wright-Patterson AFB OH, September 2009.

[29] Pérez, D.J., A.P. Crósta, C.R. Souza Filho, and G Marín. "Mineral Mapping Exploration using Hyperspectral AVIRIS Data in Los Menucos Area, Rio Negro Province (67 51'-40 53'S) Argentina".

[30] Poskosky, Kieth R. *Design of a Monocular Multi-Spectral Akin Detection, Melanin Estimation, and False Alarm Supression System*. Master's thesis, Graduate School of Engineering, Air Force Institute of Technology(AETC), 2010.

[31] Priest, Richard G. and Steven R. Meier. "Polarimetric microfacet scattering theory with applications to absorptive and reflective surfaces". *Optical Engineering*, 41(5):988–993, 2002.

[32] Rice, A.C, J.R Vasquez, Kerekes John, and M.J Mendenhall. "Persistent hyperspectral adaptive multi-modal feature-aided tracking". *NUmerica Coorporation and Rochester Institute of Technology*, 2009.

[33] Sandford, B. and L. Robertson. "Infrared Reflectance Properties of Aircraft Paint". *In Proc. IRIS Targets, Backgrounds and Discrimination*, 111, 1985.

[34] Schlick, Christophe. "An inexpensive BRDF Model for Physically-based Rendering". *Computer Graphics Forum*, 13(3):233–246, 1994.

[35] Schott, John R. *Remote Sensing The Image Chain Approach*. Oxford University Press, New York, New York, 2007.

[36] Shell, J.R. *Bidirectional reflectance: An overview with remote sensing applications and measurement recommendations*. Technical report, Rochester, New York, 2004.

[37] Stephen R. Marschner, Eric P.F Lafortune Kenneth E. Torrance, Stephen H. Westin and Donald P. Greenberg. "Image-based BRDF measurement including human skin". *Eurographics Workshop on Rendering*, 1999.

[38] Torrance, K.E. and E.M. Sparrow. "Theory for off specular reflection from roughened surface". *Journal of the OpticalSociety of America*, 57(9):1105–1114, 1967.

[39] Ward, Gregory J. "Measureing and Modeling Anisotropic Reflection". *Computer Graphics*, 26(2):1–8, 1992.

[40] Weyrich, Tim, Wojciech Matusik, Hanspeter Pfister, Bernd Bickel, Craig Donner, Chien Tu, Janet Mcandless, Jinho Lee, Addy Ngan, Henrik Wann, and Jensen Markus Gross. "Analysis of human faces using a measurement-based skin reflectance model". *ACM Transactions on Graphics*, 25:1013–1024, 2006.

www.manaraa.com

[41] Weyrich, Tim, Wojciech Matusik, Hanspeter Pfister, Jinho Lee, Addy Ngan, Henrik Wann, and Jensen Markus Gross. *A measurement-based skin reflectance model for face*. Technical report, MitsubishiElectric Research Laboratories, 2005.

www.manaraa.com

REPORT DOCUMENTATION PAGE

Form Approved
OMB No. 0704–0188

The public reporting burden for this collection of information is estimated to average 1 hour per response, including the time for reviewing instructions, searching existing data sources, gathering and maintaining the data needed, and completing and reviewing the collection of information. Send comments regarding this burden estimate or any other aspect of this collection of information, including suggestions for reducing this burden to Department of Defense, Washington Headquarters Services, Directorate for Information Operations and Reports (0704–0188), 1215 Jefferson Davis Highway, Suite 1204, Arlington, VA 22202–4302. Respondents should be aware that notwithstanding any other provision of law, no person shall be subject to any penalty for failing to comply with a collection of information if it does not display a currently valid OMB control number. **PLEASE DO NOT RETURN YOUR FORM TO THE ABOVE ADDRESS.**

1. REPORT DATE *(DD–MM–YYYY)*	2. REPORT TYPE	3. DATES COVERED *(From — To)*
24–03–2011	Master's Thesis	Jun 2009 — Mar 2011

4. TITLE AND SUBTITLE

A Multispectral Bidirectional Reflectance Distribution Function Study of Human Skin for Improved Dismount Detection

5a. CONTRACT NUMBER

-

5b. GRANT NUMBER

-

5c. PROGRAM ELEMENT NUMBER

-

6. AUTHOR(S)

Bradley M. Koch, Capt, USAF

5d. PROJECT NUMBER

10ENG300

5e. TASK NUMBER

-

5f. WORK UNIT NUMBER

-

7. PERFORMING ORGANIZATION NAME(S) AND ADDRESS(ES)

Air Force Institute of Technology
Graduate School of Engineering and Management (AFIT/EN)
2950 Hobson Way
WPAFB OH 45433-7765

8. PERFORMING ORGANIZATION REPORT NUMBER

AFIT/GE/ENG/11-22

9. SPONSORING / MONITORING AGENCY NAME(S) AND ADDRESS(ES)

Air Force Research Labs (Julia Parakkat)
2800 Q Street, B824
WPAFB, USA 45433
937-255-0605, Julia.Parakkat@wpafb.af.mil

10. SPONSOR/MONITOR'S ACRONYM(S)

AFRL/RHPA

11. SPONSOR/MONITOR'S REPORT NUMBER(S)

12. DISTRIBUTION / AVAILABILITY STATEMENT

Approval for public release; distribution is unlimited.

13. SUPPLEMENTARY NOTES

"This material is declared a work of the U.S. Government and is not subject to copyright protection in the United States."

14. ABSTRACT In 2008, the Sensors Exploitation Research Group at the Air Force Institute of Technology began using spectral properties of skin for the detection and classification of humans. Since then a multispectral skin detection system was developed to exploit the optical properties of human skin at wavelengths in the visible and near infrared region of the electromagnetic spectrum. A rules-based detector, analyzing an image spectrally, currently bases its skin pixel selection criteria on a diffuse skin reflectance model. However, when observing skin in direct view of the sun, a glint of light off skin is common and indicates specularity. The areas of skin with a high degree of specular reflectance, results in misdetections. We show that skin is characterized by diffuse and specular reflectance, with both components dependent on the scene configuration. While we cannot always rely on the person to directly face the camera or have constant illumination conditions, it is important to have flexibility with the rules-based detector as the scene changes. Our research better characterizes skin reflectance as a function of source and detector angular locations to improve on the rules-based detector.

15. SUBJECT TERMS

BRDF, Skin Detection, Dismount detection

16. SECURITY CLASSIFICATION OF:			17. LIMITATION OF ABSTRACT	18. NUMBER OF PAGES	19a. NAME OF RESPONSIBLE PERSON
a. REPORT	b. ABSTRACT	c. THIS PAGE			Michael J Mendenhall, Maj, USAF (ENG)
U	U	U	UU	105	19b. TELEPHONE NUMBER *(include area code)* (937)255 -3636,; Michael.Mendenhall@afit.edu

www.manaraa.com